2011-07-06

Structures of Poliovirus and Antibody Complexes Reveal Movements of the Capsid Protein VP1 During Cell Entry

Jun Lin
Brigham Young University - Provo

Structures of Poliovirus and Antibody Complexes

Reveal Movements of the Capsid Protein VP1 During Cell Entry

Jun Lin

A dissertation submitted to the faculty of
Brigham Young University
in partial fulfillment of the requirements for the degree of

Doctor of Philosophy

David M. Belnap, chair
Bradford K. Berges
Gregory F. Burton
Allen R. Buskirk
Steven R. Herron

Department of Chemistry and Biochemistry

Brigham Young University

August 2011

ABSTRACT

Structures of Poliovirus and Antibody Complexes
Reveal Movements of the Capsid Protein VP1 During Cell Entry

Jun Lin
Department of Chemistry and Biochemistry, BYU
Doctor of Philosophy

In the infection process, native poliovirus (160S) first converts to a cell-entry intermediate (135S) particle, which causes the externalization of capsid proteins VP4 and the N-terminus of VP1 (residues 1-53). The externalization of these entities is followed by release of the RNA genome, leaving an empty (80S) particle. Three antibodies were utilized to track the location of VP1 residues in different states of poliovirus by cryogenic electron microscopy (cryo-EM).

"P1" antibody binds to N-terminal residues 24-40 of VP1. Three-dimensional reconstruction of 135S-P1 showed that P1 binds to a prominent capsid peak known as the "propeller tip". In contrast, our initial 80S-P1 reconstruction showed P1 Fabs also binding to a second site, ~60 Å distant, at the icosahedral twofold axes. Analysis of 80S-P1 reconstructions showed that the overall population of 80S-P1 particles consisted of three kinds of capsids: those with P1 Fabs bound only at the propeller tips; only at the twofold axes; or simultaneously at both positions. Our results indicate that, in 80S particles, a significant fraction of VP1 can deviate from icosahedral symmetry. Similar deviations from icosahedral symmetry may be biologically significant during other viral transitions.

"C3" antibody binds to 93-103 residues (BC loop) of VP1. The C3 epitope shifts outwards in radius by 4.5% and twists through 15° in the 160S-to-135S transition, but appears unchanged in the 135S-to-80S transition. In addition, binding of C3 to either 160S or 135S particles causes residues of the BC loop to move an estimated 5 ($\pm$2) Å, indicating flexibility. The flexibility of BC loop may play a role in cell-entry interactions.

At 37 °C, the structure of poliovirus is dynamic, and internal polypeptides VP4 and the N-terminus of VP1 externalize reversibly. An antibody, binding to the residues 39-55 of VP1, was utilized to track the location of the N-terminus of VP1 in 160S particle in the "breathing" state. The resulting reconstruction showed the capsid expands similarly to the irreversibly altered 135S particle, but the N-terminus of VP1 is located near the twofold axes, instead of the propeller tip as in 135S particles.

ACKNOWLEDGEMENTS

Table of Contents

List of Tables

List of Figures

Chapter 1. Introduction

1.1 Cell Entry of Non-Enveloped Viruses

For animal viruses to effectively initiate infection into a host cell, they must bind to an appropriate cell-surface receptor and then deliver their nucleic acid to the appropriate cellular compartment. Enveloped viruses such as human immunodeficiency virus (HIV) and influenza virus deliver their genome by fusing the viral membrane with the host cell membrane at the cell surface or within endocytic vesicles. Non-enveloped viruses must provide another mechanism to allow their protein-encased genomes to enter their hosts. These mechanisms are thought to be either endosomal lysis or pore formation (*1, 2*). For the most part, the cell-entry mechanisms of non-enveloped virus are not well understood. However, cryo-EM analysis of polioviruses has provided some detailed information on structural changes during cell entry (*3-7*).

1.2 Picornavirus Structure and Cell Entry

Picornaviruses are small, icosahedral, non-enveloped viruses with a single positive strand RNA genome. The fundamental picornavirus capsid architecture is the same in all members and is composed of 60 copies of each of four structural proteins, VP1 to VP4, arranged with icosahedral symmetry. VP1, VP2, and VP3 form the outer surface of the capsid, having eight stranded antiparallel β-sheet structures with a "jelly roll" topology. VP4 lies in an extended conformation on the inner surface of the capsid (Fig. 1.1).
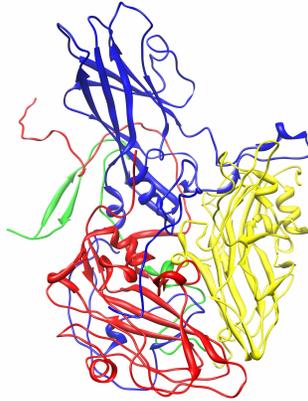
Figure 1.1 The crystal structure of the poliovirus capsid proteins (*8*). One asymmetric unit shows ribbon diagrams of VP1 (blue), VP2 (yellow), VP3 (red), and VP4 (green). The outer surface faces the reader.

During cell entry, picornaviruses at first attach to the cell via an interaction with specific receptors on the cell membrane. The next step of picornavirus infection is uncoating, where the viral capsid forms an opening to release the genome into the infected cell. Although cell entry and uncoating remains poorly understood, the cell entry of poliovirus is understood better than that of any other picornavirus.

1.3 Poliovirus Structure and Cell Entry

Poliovirus, the prototypic member of the picornavirus family, causes poliomyelitis. Poliovirus is an excellent model system to study non-enveloped cell-entry mechanisms because 1) procedures for cultivating the virus and its cellular receptor (poliovirus receptor or CD155) are well established, 2) both the virus and receptor are well characterized and 3) the structures of poliovirus in different states are known (*3-5, 7-11*). The viral surface is dominated by (i) star-shaped mesas at the fivefold axes surrounded by deep canyons and (ii) three-bladed propellers at the threefold axes separated by saddle-like depressions straddling the twofold axes (Fig. 1.2).
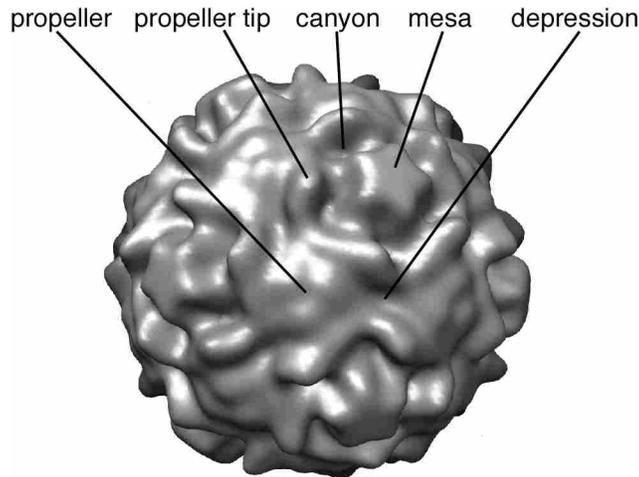
Figure 1.2 Prominent structural features on the exterior of native poliovirus (*3*). The mesa is formed solely by VP1, the canyon and propeller by VP1, VP2, and VP3. The propeller tip is formed by the EF loop of VP2 and flanking polypeptide sequences from VP1 and VP3. Each mesa is centered on a fivefold symmetry axis, each propeller is centered on a threefold symmetry axis, and each saddle-like depression is centered on a twofold symmetry axis.

Cell-entry of poliovirus is thought to occur via a pore opening as a result of exposure to membrane-binding entities from the capsid (*2, 4, 11, 12*). The virion (sedimentation coefficient, 160S) interacts with its receptor CD155 at the canyon (Fig.1.3) (*10*) and changes into the cell-entry intermediate (135S) form. The receptor appears to act as a catalyst (*2, 13*). VP4, a protein that is known to form membrane channels in vitro (*14*), and the N-terminus of VP1, an entity known to interact with lipid vesicles (*12*), are irreversibly externalized in the transition from 160S to 135S forms. The hypothesis is that the intermediate particle interacts with the membrane, a channel is formed, and then RNA enters the cell (Fig. 1.4). After releasing the RNA into the infected cell, poliovirus sediments at 80S.

Other closely related picornaviruses such as rhinoviruses, echoviruses, coxsackieviruses, and enteroviruses are thought to use similar cell-entry mechanisms (*18*).
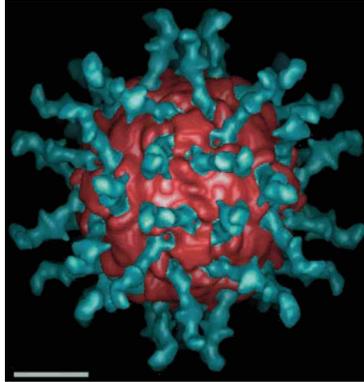
Figure 1.3 Structure of poliovirus-CD155 complex (*10*). Cryo-EM reconstruction of poliovirus (red) and the ectodomain of CD155 (cyan). Bar =100 Å.
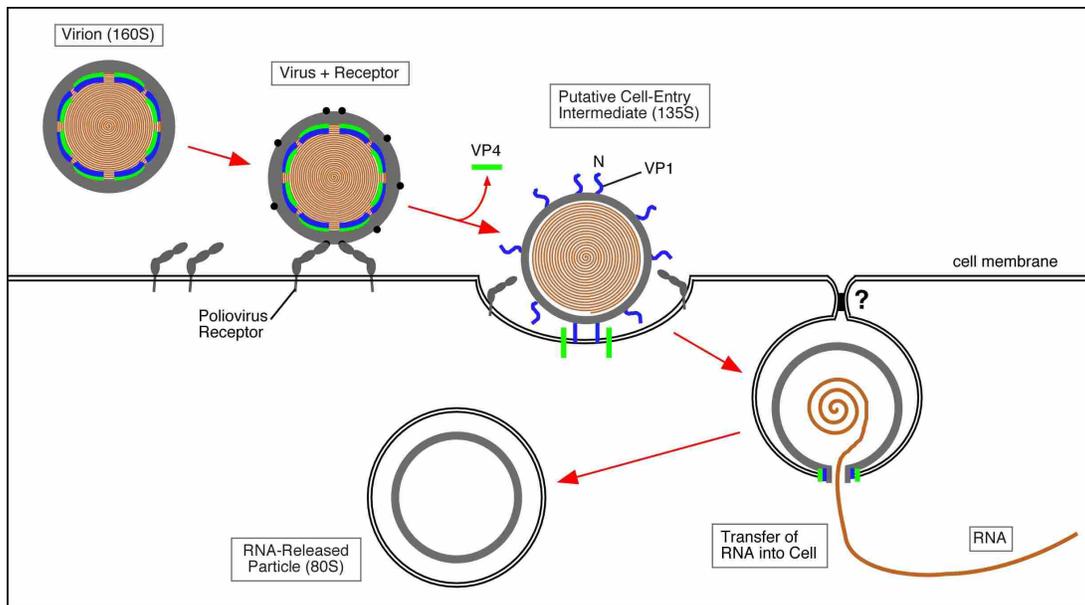
Figure 1.4 Model of cell entry for poliovirus by Dr. David M. Belnap from references (*2, 4, 15-17*). This model also is proposed for the other picornaviruses closely related to poliovirus, though cell entry in those related viruses could occur at the cell membrane or through an endosomal membrane that has penetrated deeper into the cell. Poliovirus virion (sedimentation coefficient = 160S) interacts with poliovirus receptor. The black dots represent the receptor binding sites. This interaction catalyzes a conformational change to the cell-entry intermediate particle (sedimentation coefficient = 135S). VP4 and the N-terminus of VP1, which are internal in the 160S particle, are irreversibly externalized in the transition to 135S particle. The two externalized entities allow the 135S particle to interact with the cell membrane. The virus particle is enclosed within a vesicle or is in a membrane invagination that is sealed from the extracellular environment. Then, a channel forms connecting the interior of the virus and the

cytoplasm, and the RNA is injected into the cytoplasm. The force driving RNA release is unknown. RNA release (uncoating) occurs within approximately 200 nm of the cell membrane, so the vesicle may still be attached to the cell membrane. The observed RNA-released particle (sedimentation coefficient = 80S) is thought to be the final state of the virus particle after entry. 160S, 135S, 80S, and virus-receptor complexes have been structurally characterized for poliovirus (*3-5, 7-11*).

1.3.1 Poliovirus "Breathing" State

"Breathing" means transient, reversible changes in protein conformation. Several nonenveloped viruses have been shown to undergo "capsid breathing" (see Chapter 5). "Breathing" of poliovirus was first discovered when antibodies to internal, unexposed amino-acid sequences were found to bind to native particles (*19, 20*). These epitopes are part of the membrane-binding entities irreversibly exposed during cell entry. The studies showed that "capsid breathing" might actually represent large dynamic changes in virion structure. The "breathing" of some viruses is easier to observe at higher temperatures. For example, "breathing" of the poliovirus capsid occurs at 37 ºC but not at 25 ºC (*19, 21*) and "breathing" of the human rhinovirus 16 capsid occurs at 25 ºC but not at 4 ºC (*22*). If "breathing" is important for picornavirus cell entry then presumably it includes conformational changes necessary for receptor-binding, cell-entry, and the eventual triggering of genomic release (uncoating) in many or all non-enveloped viruses. The transient exposure of internal proteins may be an important step for the cell-entry process, especially the conformational changes required to insert internal, hydrophobic, membrane-binding peptides into the membrane. Antiviral agents, antibodies, or mutations, which can block viral "breathing", can prevent viral infection (*21, 23-25*). Whether the reversible changes in "breathing" are similar to the irreversible changes that occur during cell entry is an important question, and Chapter 5 will provide some information about this question.

1.3.2 Poliovirus Intermediate

The 160S particle interacts with CD155 on the host cell and changes into the intermediate 135S particle. The formation of 135S particles of poliovirus can be induced (*11*) by membrane extracts (*26*), solubilized receptor (*27, 28*), soluble ectodomains of the receptor (*29, 30*), or by heat treatment (*31*). The 160S-to-135S transition includes the externalization of VP4 and the N-terminus of VP1. One early poliovirus entry model suggests that receptor binding induces changes that widen the channel at the fivefold axes, allowing VP4, the N-terminus of VP1, and the viral RNA to exit the capsid at the particle fivefold axes (Fig. 1.5 A, B) (*32-34*). The location of the N-terminus of VP1 in the intermediate (135S) particle will give evidence to verify or modify the entry model. In the 135S particles, the V8 protease of *Staphylococcus aureus* specifically cleaves after a glutamate at position 31 of VP1 and a V8-proteolyzed 135S particle cryo-EM reconstruction was obtained (*4*). By comparing the 135S structure with the V8-proteolyzed 135S structure, Bubeck et al. found that the N-terminus of VP1 is located at the propeller tip, near the canyon. Based on the new finding that the N-terminus of VP1 does not exit the capsid at the fivefold axis, but near the canyon, an alternative model for poliovirus entry was suggested (Fig.1.5 A,C,D) (*4*).
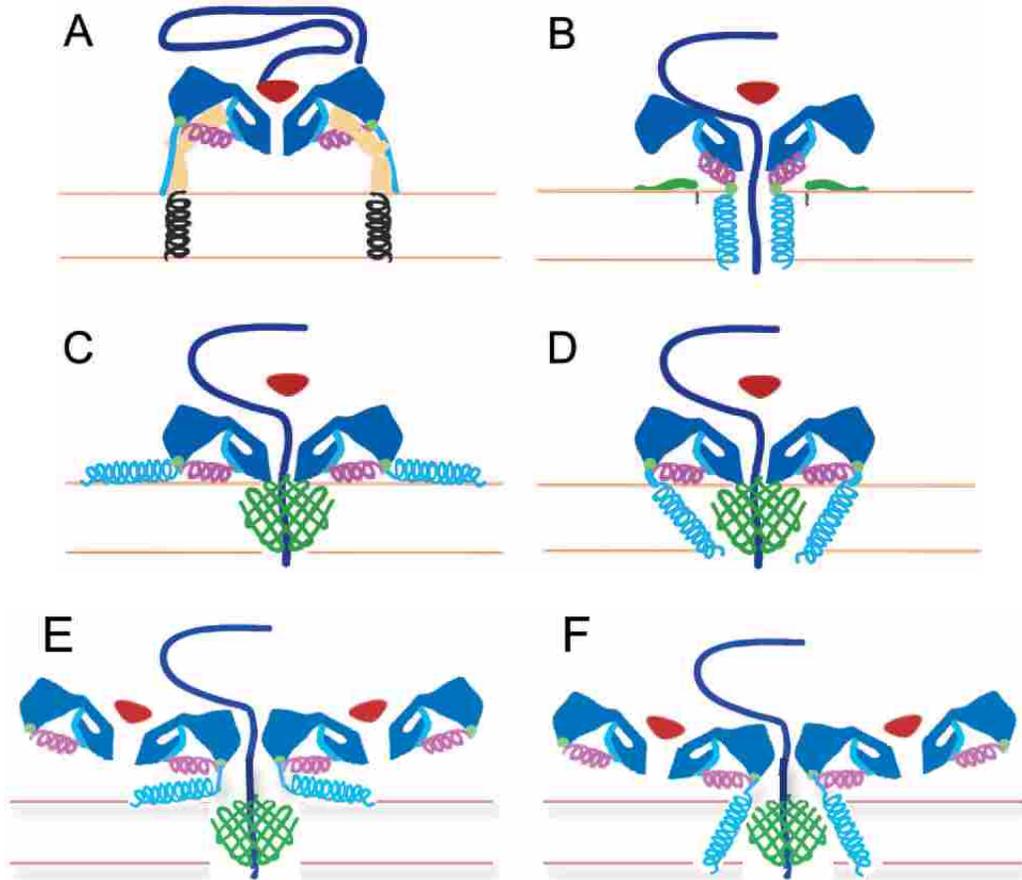
Figure 1.5 Working models for poliovirus entry (A-D from (*4*) and E-F are adapted from Bubeck et. al. (*4*) encoding the concept that RNA exits from 2-fold axis (*7*). A cross section of a portion of the capsid is shown in dark blue, VP4 is green, and the N-terminus of VP1 is cyan and magenta. The V8 cleavage site is shown as a green circle. (A) Native poliovirus binds its receptor, Pvr (ectodomains 1 to 3, tan; transmembrane domain, black helix), and at physiological temperature undergoes an irreversible change to the 135S particle. The path of egress of the N-terminus of VP1, suggested by the 135S reconstruction (*4*), would not preclude the continued binding of Pvr. (B to F) Alternative models for the direct anchoring of the virus to the membrane via the N-terminus of VP1 and formation of a transmembrane pore for RNA translocation. (B to D) RNA exits at a fivefold axis. The VP3 tube (red) blocks an otherwise open channel along the fivefold axis. To accommodate the passage of RNA (purple), the VP3 tube has shifted, and the channel has expanded, becoming continuous with a pore through the membrane. (E and F) are adapted from (C and D) (*4, 7*) RNA exits near a twofold axis between 2 propeller tips. The VP3 tube at the fivefold axis helps fix the relative position between viral proteins and helps keep the capsid rigid, In this model, because RNA does not exit at a fivefold axis, VP3 tube does not shift, which is consist with the VP3 tube in stable in

all states of poliovirus (*2*). (B) Amphipathic helices at the N-terminus of VP1 (cyan) may form a five-helix bundle close to the fivefold axis, which would require the magenta helix to dissociate from the body of the virus. Alternatively, VP4 may play a more central role in pore formation (C to F). In that case, VP1 may participate directly in forming the pore (D and F) or serve as a nonspecific membrane anchor (C and E).

1.3.3 Empty Poliovirus

The empty 80S particles are thought to be the final state of poliovirus in its cell-entry process. Recently, the Hogle lab at Harvard Medical School found that at least three states of 80S particles exist: the early RNA-releasing form (80S.e) (*6*), the RNA-releasing form caught in the act of releasing RNA (80S "caught in act") (Fig. 1.6) (*7*), and the late RNA-releasing form (80S.l) (*6*). The 80S "caught in act" map showed that RNA exits near the 2-fold axis toward each neighboring 5-fold axis, and not at the 5-fold axis as has been suggested previously (*7, 11*).

Fig.1.6 A surface representation of two virions caught in the process of genome release (*7*). Icosahedral averaging was applied only to the capsid region (green). An isocontour surface of the RNA density is rendered in red.

Based on this new finding, that viral genome exits near the 2-fold axis, not from the 5-fold axis, I modified the model for poliovirus entry, proposed by Bubeck et al. in 2005 (Fig. 1.5 C,D), and hypothesize another alternative poliovirus entry model (Fig. 1.5 E,F): Receptor binding induces 160S to 135S conformational changes that allowing VP4 and the N-terminus of VP1 exit at the propeller tip near the canyon (as in the previous model). The externalized VP4

and the N-terminus of VP1 forms a channel between two propeller tips near the twofold axis, and the viral RNA exits the capsid near the particle twofold axes.

1.4 Disease Prevention and Treatment

Structural analysis to understand the virus itself, its interactions with host cell receptors and antibodies, and viral cell entry is important for virus disease prevention and treatment, for example, vaccination and antiviral drugs (*35, 36*). Some viral diseases can be controlled and prevented by vaccination with low cost. For picornavirus-associated diseases, vaccines have been developed for poliomyelitis, hepatitis A, and foot-and-mouth disease (*35*). Synthetic peptides from the immunogenic sequences of capsid proteins potentially could be used as vaccines, and the antibodies induced by the synthetic peptides may block cell entry, e.g. prevent the sequence from binding to the cellular receptor (*37*). Antiviral drugs could be inhibitors of attachment, entry, uncoating, or replication (*36*). For picornaviruses, one of the most well-characterized examples are the capsid protein VP1 and viral drugs that prevent viral uncoating (*36*). The WIN compounds bind poliovirus into the hydrophobic pocket, which is located underneath the canyon floor. WIN compounds stabilize the capsid, preventing conformational change (to the cell-entry intermediate) (*36*).

References

1. Smith, A. E., and Helenius, A. (2004) How viruses enter animal cells, *Science 304*, 237-242.

2. Hogle, J. M. (2002) Poliovirus cell entry: common structural themes in viral cell entry pathways, *Annu. Rev. Microbiol. 56*, 677-702.

3. Belnap, D. M., Filman, D. J., Trus, B. L., Cheng, N., Booy, F. P., Conway, J. F., Curry, S., Hiremath, C. N., Tsang, S. K., Steven, A. C., and Hogle, J. M. (2000) Molecular tectonic model of virus structural transitions: the putative cell entry states of poliovirus, *J. Virol. 74*, 1342-1354.

4. Bubeck, D., Filman, D. J., Cheng, N., Steven, A. C., Hogle, J. M., and Belnap, D. M. (2005) The structure of the poliovirus 135S cell entry intermediate at 10-Angstrom resolution reveals the location of an externalized polypeptide that binds to membranes, *J. Virol. 79*, 7745-7755.

5. Bubeck, D., Filman, D. J., and Hogle, J. M. (2005) Cryo-electron microscopy reconstruction of a poliovirus-receptor-membrane complex, *Nat Struct Mol Biol 12*, 615-618.

6. Levy, H. C., Bostina, M., Filman, D. J., and Hogle, J. M. (2010) Catching a virus in the act of RNA release: a novel poliovirus uncoating intermediate characterized by cryo-electron microscopy, *J Virol 84*, 4426-4441.

7. Bostina, M., Levy, H., Filman, D. J., and Hogle, J. M. (2011) Poliovirus RNA is released from the capsid near a twofold symmetry axis, *J. Virol. 85*, 776-783.

8. Wien, M. W., Curry, S., Filman, D. J., and Hogle, J. M. (1997) Structural studies of poliovirus mutants that overcome receptor defects, *Nature Struct. Biol. 4*, 666-674.

9. Hogle, J. M., Chow, M., and Filman, D. J. (1985) Three-dimensional structure of poliovirus at 2.9 Å resolution, *Science 229*, 1358-1365.

10. Belnap, D. M., McDermott, B. M., Jr., Filman, D. J., Cheng, N., Trus, B. L., Zuccola, H. J., Racaniello, V. R., Hogle, J. M., and Steven, A. C. (2000) Three-dimensional structure of poliovirus receptor bound to poliovirus, *Proc. Natl. Acad. Sci. USA 97*, 73-78.

11. Levy, H., Bostina, M., Filman, D. J., and Hogle, J. M. (2010) Cell Entry: A Biochemical and Structural Perspective, In *The Picornaviruses* (Ehrenfeld, E., Domingo, E., and Roos, R. P., Eds.), pp 87-104, ASM Press, Washington, DC.

12. Fricks, C. E., and Hogle, J. M. (1990) Cell-induced conformational change in poliovirus: externalization of the amino terminus of VP1 is responsible for liposome binding, *J. Virol. 64*, 1934-1945.

13. Racaniello, V. R. (1996) The poliovirus receptor: a hook, or an unzipper?, *Structure 4*, 769-773.

14. Danthi, P., Tosteson, M., Li, Q.-h., and Chow, M. (2003) Genome delivery and ion channel properties are altered in VP4 mutants of poliovirus, *J. Virol. 77*, 5266-5274.

15. Ansardi, D. C., Porter, D. C., Anderson, M. J., and Morrow, C. D. (1996) Poliovirus assembly and encapsidation of genomic RNA, *Adv Virus Res 46*, 1-68.

16. Tuthill, T. J., Bubeck, D., Rowlands, D. J., and Hogle, J. M. (2006) Characterization of early steps in the poliovirus infection process: receptor-decorated liposomes induce conversion of the virus to membrane-anchored entry-intermediate particles, *J Virol 80*, 172-180.

17. Brandenburg, B., Lee, L. Y., Lakadamyali, M., Rust, M. J., Zhuang, X., and Hogle, J. M. (2007) Imaging poliovirus entry in live cells, *PLoS Biol 5*, e183.

18. Hewat, E. A., Neumann, E., and Blaas, D. (2002) The concerted conformational changes during human rhinovirus 2 uncoating, *Mol Cell 10*, 317-326.

19. Li, Q., Yafal, A. G., Lee, Y. M., Hogle, J., and Chow, M. (1994) Poliovirus neutralization by antibodies to internal epitopes of VP4 and VP1 results from reversible exposure of these sequences at physiological temperature, *J Virol 68*, 3965-3970.

20. Roivainen, M., Piirainen, L., Rysa, T., Narvanen, A., and Hovi, T. (1993) An immunodominant N-terminal region of VP1 protein of poliovirion that is buried in crystal structure can be exposed in solution, *Virology 195*, 762-765.

21. Dove, A. W., and Racaniello, V. R. (2000) An antiviral compound that blocks structural transitions of poliovirus prevents receptor binding at low temperatures, *J Virol 74*, 3929-3931.

22. Katpally, U., Fu, T. M., Freed, D. C., Casimiro, D. R., and Smith, T. J. (2009) Antibodies to the buried N terminus of rhinovirus VP4 exhibit cross-serotypic neutralization, *J Virol 83*, 7040-7048.

23. Lewis, J. K., Bothner, B., Smith, T. J., and Siuzdak, G. (1998) Antiviral agent blocks breathing of the common cold virus, *Proc Natl Acad Sci U S A 95*, 6774-6778.

24. Reisdorph, N., Thomas, J. J., Katpally, U., Chase, E., Harris, K., Siuzdak, G., and Smith, T. J. (2003) Human rhinovirus capsid dynamics is controlled by canyon flexibility, *Virology 314*, 34-44.

25. Broo, K., Wei, J., Marshall, D., Brown, F., Smith, T. J., Johnson, J. E., Schneemann, A., and Siuzdak, G. (2001) Viral capsid mobility: a dynamic conduit for inactivation, *Proc Natl Acad Sci U S A 98*, 2274-2277.

26. De Sena, J., and Mandel, B. (1976) Studies on the in vitro uncoating of poliovirus. I. Characterization of the modifying factor and the modifying reaction, *Virology 70*, 470-483.

27. Gomez Yafal, A., Kaplan, G., Racaniello, V. R., and Hogle, J. M. (1993) Characterization of poliovirus conformational alteration mediated by soluble cell receptors, *Virology 197*, 501-505.

28. Kaplan, G., Freistadt, M. S., and Racaniello, V. R. (1990) Neutralization of poliovirus by cell receptors expressed in insect cells, *J Virol 64*, 4697-4702.

29. Arita, M., Koike, S., Aoki, J., Horie, H., and Nomoto, A. (1998) Interaction of poliovirus with its purified receptor and conformational alteration in the virion, *J Virol 72*, 3578-3586.

30. Tsang, S. K., McDermott, B. M., Racaniello, V. R., and Hogle, J. M. (2001) Kinetic analysis of the effect of poliovirus receptor on viral uncoating: the receptor as a catalyst, *J Virol 75*, 4984-4989.

31. Curry, S., Chow, M., and Hogle, J. M. (1996) The poliovirus 135S particle is infectious, *J Virol 70*, 7125-7131.

32. Giranda, V. L., Heinz, B. A., Oliveira, M. A., Minor, I., Kim, K. H., Kolatkar, P. R., Rossmann, M. G., and Rueckert, R. R. (1992) Acid-induced structural changes in human rhinovirus 14: possible role in uncoating, *Proc Natl Acad Sci U S A 89*, 10213-10217.

33. Hewat, E. A., and Blaas, D. (2004) Cryoelectron microscopy analysis of the structural changes associated with human rhinovirus type 14 uncoating, *J Virol 78*, 2935-2942.

34. Kolatkar, P. R., Bella, J., Olson, N. H., Bator, C. M., Baker, T. S., and Rossmann, M. G. (1999) Structural studies of two rhinovirus serotypes complexed with fragments of their cellular receptor, *EMBO J 18*, 6249-6259.

35. Rowlands, D. J., and Minor, P. D. (2010) Vaccine Strategies, In *The Picornaviruses* (Ehrenfeld, E., Domingo, E., and Roos, R. P., Eds.), pp 431-447, ASM Press, Washington, DC.

36. De Palma, A. M., and Neyts, J. (2010) Antiviral Drugs, In *The Picornaviruses* (Ehrenfeld, E., Domingo, E., and Roos, R. P., Eds.), pp 461-482, ASM Press, Washington, DC.

37. Ivanov, V. T., Volpina, O. M., Surovoi, A. Y., Volkova, T. D., Kozhich, A. T., and Tchikin, L. D. (1990) Towards Synthetic Antiviral Vaccines, *Pure and Applied Chemistry 62*, 1433-1436.

Chapter 2. Cryo-Electron Microscopy Reconstruction

2.1 Biological Macromolecular Structure

X-ray crystallography, nuclear magnetic resonance (NMR) and three-dimensional electron microscopy (3DEM) are three major methods used to solve biological macromolecular structure. The structures determined by X-ray crystallography and NMR usually are at atomic resolution— 3DEM structures usually are not. However, X-ray crystallography and NMR have significant limitations: A single crystal of a large biological molecule or macromolecular complex may be very hard to grow, and the crystal form of the molecule may not be in the biologically active state. Typically, NMR can only solve molecules less than 20 kDa in size. 3DEM, especially images obtained by cryogenic electron microscopy (cryo-EM), can be used to determine the 3D structures of large biological macromolecules with a molecular weight more than 200 kDa. For one EM grid sample preparation, less than 1 pmol is sufficient.

2.2 Transmission Electron Microscopy

Transmission electron microscopy (TEM) is a microscopy technique whereby a beam of electrons is transmitted through an ultra-thin specimen. As it passes through the specimen, the beam interacts with the specimen. This interaction creates an image; the image is magnified and focused onto an imaging device such as a fluorescent screen, a layer of photographic film, or a CCD camera.

2.3 EM Specimen Preparation Methods

2.3.1 Negative Staining

Brenner and Horne first applied the negative-staining method to observe tobacco mosaic virus and turnip yellow mosaic virus (*1*). A solution of 1–2 % uranyl acetate is a typical negative staining solution. The sample solution is placed on an electron-microscope grid coated with evaporated carbon. After the sample is blotted with filter paper, the sample is coated by uranyl acetate, which provides high contrast and sample protection. The negative staining method is frequently applied to obtain high contrast images of the particle. This method is quick and relative simple, and in my work, it was used as an important first step to obtain preliminary data of a virus sample. Usually, before preparation of a cryo-EM specimen, a sample is checked by negative staining to make sure that the sample itself and the solution conditions (e.g. the concentration, pH value, buffer solution, and the ion strength) are suitable for cryo-EM sample preparation.

Negative stain can introduce artifacts, such as "one-sidedness" and particle flattening. Sometimes, only one side, e.g. the bottom, will be stained. As the layer of stain dries, specimens can be flattened by surface-tension forces.

2.3.2 Cryo-EM

Cryo-EM is electron microscopy of a hydrated sample that is frozen at cryogenic temperatures (liquid nitrogen or liquid helium temperatures). A solution of biological macromolecules is loaded into the pores of a perforated carbon-coated grid and the molecules are embedded in amorphous ice by rapid freezing of a sample made thin by blotting. Cryo-EM is a direct and important method for determining the structures of large biological molecules.

Radiation damage and the high vacuum in the EM column are two major problems that needed to be solved to record electron micrographs of biological specimens. In 1984 at the European Molecular Biology Laboratory, Jacques Dubochet and coworkers first introduced a practical application of cryo-EM. They published in *Nature* images of adenovirus imbedded in a vitrified layer of water (*2*). The problem of the high vacuum was solved by embedding the sample in vitreous ice at cryogenic temperature (such as liquid nitrogen or liquid helium). To diminish the effect of radiation damage, a very low dose of electrons was used to image the cryo-EM sample. Since that time, the cryo-EM technique was used with 3DEM methods to produce three-dimensional structures. These and other developments have made 3D cryo-EM a routine technique for the structural analysis of biological molecules, especially large macromolecules.

Besides obtaining a static molecular structure, cryo-EM can be used to solve dynamic or kinetic molecular structure. The major advantage of cryo-EM is that molecules are in their native state (not fixed or stained). At selected time intervals, temperatures, or chemical conditions, samples can be quickly frozen to capture macromolecular complexes in different functional states. X-ray crystallography and NMR only provide signals from the entire sample, but for cryo-EM, individual molecular images can be selected from a population and be classified into different groups to demonstrate the structures of different conformations within the population (such as the classification experiment in Chapter 3). A single imaged particle also can show a particular feature (such as the one-particle reconstruction experiment in Chapter 3).

2.3.3 3D Reconstruction

In the transmission electron microscope, 3D structural information is projected into two-dimensional (2D) projection images. The density at each point of a 2D projection image

represents the summation of all densities in the sample perpendicular to this projection plane (Fig. 2.1).
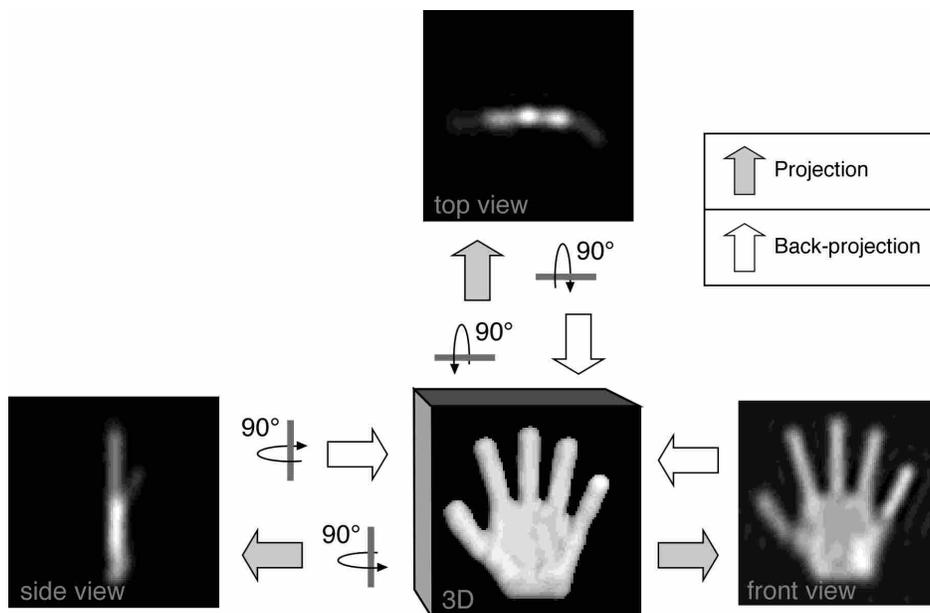
Figure 2.1 Reconstruction of a 3D structure from 2D projection images via real-space processing (*3*). Front, side, and top 2D projection images (labeled as front view, side view, and top view) were acquired by projection (gray arrows) from a model of a human left hand (labeled as 3D) with different rotations. Back-projection (white arrows) is the opposite procedure. This reverse-projection method allows the 3-D structure to be reconstructed.

From cryo-EM micrographs, 2D projection images of each particle can be acquired. Those 2D projections can be used to reconstruct the 3D structure via real-space processing or Fourier transforms (*3*). 3D structure can be achieved by "back projection" in real (Cartesian) space (Fig. 2.1) (*3*). The real-space and Fourier-transform forms of an image are interchangeable. The Fourier transform is a representation of the image in the frequency (specifically spatial frequency) dimension. The advantage of using Fourier transforms is filtering according to spatial frequency. By using different filters, low-, middle- or high-spatial frequencies can be excluded to improve a reconstruction or to aid in 3D image analysis. For example, the high spatial

frequencies contain a much higher fraction of noise than the low or middle spatial frequencies. These frequencies are of little use in image analysis or in computing the 3D reconstruction. The reconstruction done by filtering high spatial frequencies shows less noise. The projection (or central-section) theorem is the mathematical principle behind Fourier-transform reconstructions (Fig. 2.2) (*3*).
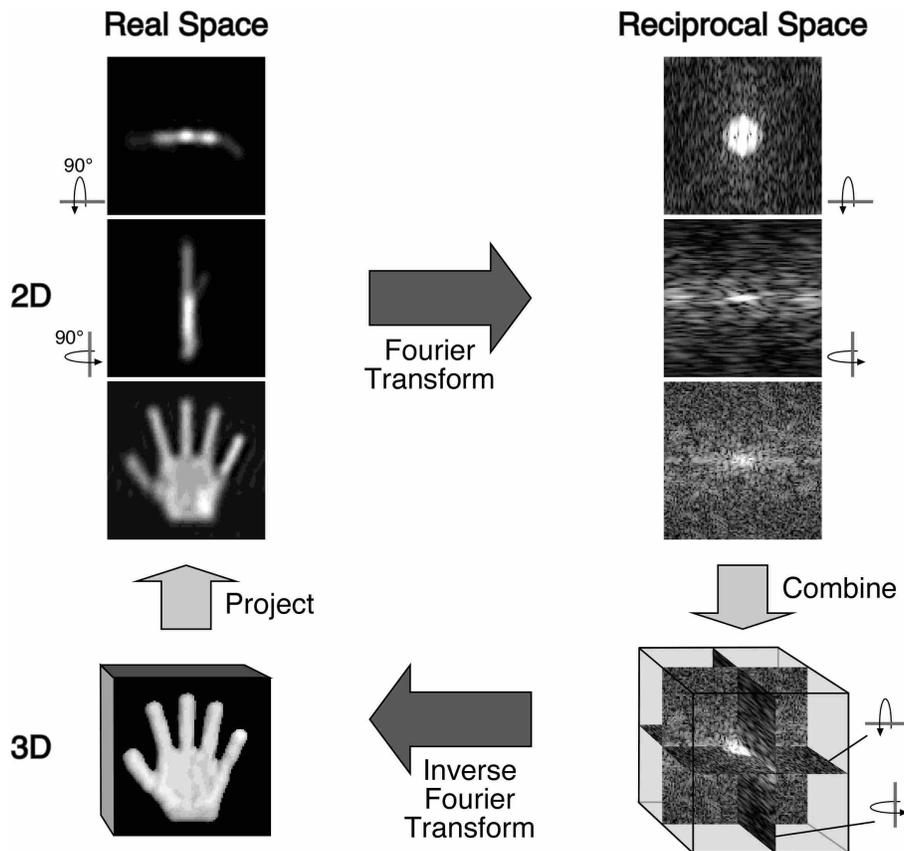
Figure 2.2 The projection theorem (*3*). Instead of back-projecting 2D projection images to obtain the 3D structure directly, 2D images are Fourier transformed, the Fourier transform of 2D images are the central slices of the 3D Fourier transform normal to the viewing direction placed in the appropriate place in the 3D transform, and the inverse Fourier transform of the 3D Fourier transform is used to convert back to real space (the 3D structure). (Note that more unique 2D projection images provide more 3D Fourier transform information to obtain a better reconstruction.)

Since 1984, cryo-EM techniques and reconstruction methods have made rapid progress. Currently, the highest resolution of a cryo-EM reconstruction is 1.9 Å (*4, 5*) which is the structure of double-layered two-dimensional aquaprin-0 crystal achieved by electron crystallography. However, most 3D cryo-EM structures have lower resolution. Three different 3DEM methods are used: single-particle analysis, electron tomography, and electron crystallography. Single-particle analysis is the primary method I used.

Single-Particle Analysis

"Single-particle" analysis is suitable to solve the 3D structure of biological macromolecules that are freestanding (non-crystalline) and have regular or consistent structure from particle to particle. The particles could be symmetric particles, such as viral capsids, or asymmetric particles, such as ribosomes. In theory, atomic resolution can be achieved if sufficient numbers of particle images are used (*6*). The sample particles have, or are assumed to have, identical 3D structure, but lie on the grid in different orientations (i.e. view directions). A large number of 2D particle images are collected, images are processed, and a 3D reconstruction obtained.

The 3D reconstruction is usually computed as follows: 2D project images of the sample particles are picked from the micrographs, and 2D images are normalized and contrast transfer function are corrected (Fig. 2.3, step 9). The origin (center of the particles) and orientation (the view direction) of each imaged particle are determined (Fig. 2.3, steps 10-12). The 3D reconstruction is calculated, then this reconstruction is used as the initial structure model for the next iteration to match and refine the origins and orientations of the imaged particles and then get a more accurate three-dimensional structure model, and these steps are repeated until the calculations converge and no improvements are observed (Fig. 2.3) (*3*). Many software packages

for single-particle analysis software exist, such as Bsoft (*7*), PFT3DR (*8-10*), EMAN (*11, 12*), SPIDER (*13, 14*), XMIPP (*15*), AUTO3DEM (*16*), FREALIGN (*17*), and IMAGIC (*18*). Bsoft and PFT3DR were used to reconstruct poliovirus-Fab maps in the following chapters. The highest resolution of a cryo-EM reconstruction by single particle analysis is 3.3 Å (*5*) and at this high resolution, the amino acid side chain densities of the aquareovirus capsid proteins are easily visible.
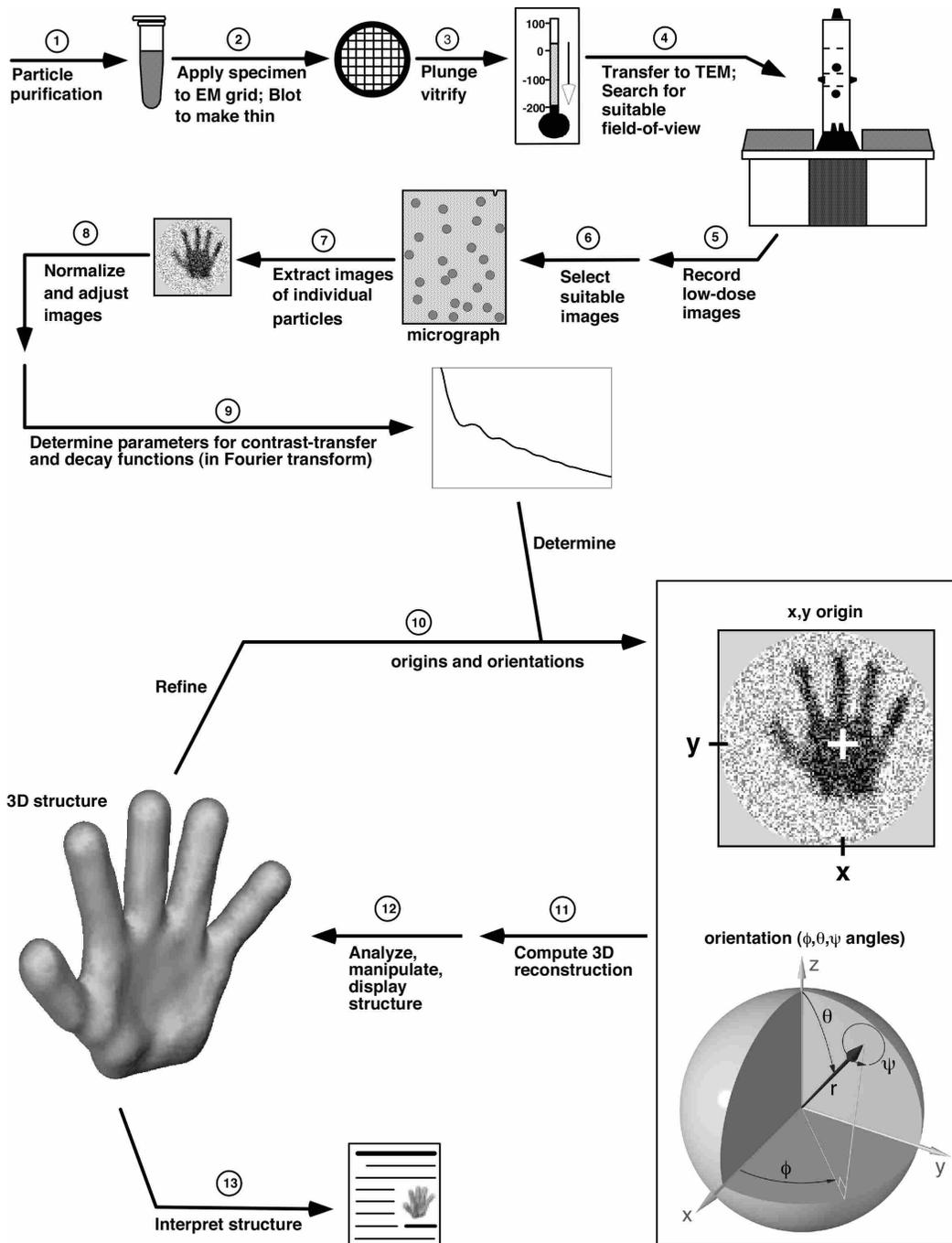
Figure 2.3 Protocol for cryo-EM 3D reconstruction (*3*). Steps 1 to 3 are sample preparation; 4 to 6, microscopy; 7 to 12, image processing; and 13, interpretation (**1**) Sample should be purified to make the sample particles distinguishable in the images. (**2**) 2 to 5 µl of sample is loaded to a carbon-coated grid and is blotted to produce a very thin aqueous film. (**3**) The specimen is plunge frozen, usually in liquid ethane, to produce vitreous ice. (**4**) The cryo-EM grid is stored in a cryo-storage dewar or transferred to TEM in a specialized "cold holder", where it is

maintained at liquid nitrogen or helium temperatures until images are recorded. The specimen is observed in TEM and images are recorded. (**5**) To protect the specimen from radiation damage, low electron dose is applied. (**6**) The recorded images are digitalized and checked to select good images with low astigmatism and drift. (**7**) Usually, each particle image is extracted for single-particle analysis. (This step may not be necessary for an electron tomography reconstruction.) (**8**) Particle images should be normalized and adjusted to be statistically similar, e.g., have same background or average value. (**9**) For cryo-EM, under-focused micrographs provide more image contrast, which also introduces image/contrast distortions. To obtain a high resolution of 3D reconstruction, this contrast transfer function (CTF) and the natural signal decay with increasing resolution can be corrected by modeling mathematically. (**10**) Translational and rotational alignments. Angles {φ, θ,ψ} and lengths {x,y} are determined (*19*). (**11**) Computation of 3D reconstruction. (**12**) Various analysis techniques may be used to assess the quality of the reconstruction. The resolution of the map usually is one criterium to determine if a reconstruction is satisfactory. To refine the origins and orientations of the imaged particles, steps 10 to 12 should be repeated until the resolution of the 3D reconstruction does not improve. (**13**) The results and interpretation of the data are written for publication.

Electron Tomography

Electron tomography is usually applied for naturally variable and/or highly complex biological structures (*20*), such as non-regular (pleiomorphic) macromolecules (*21, 22*), supramolecular heterogeneous assemblies, organelles and cellular fractions (*23*), isolated macromolecules to cells and cell sections (*3*), or macromolecules in cell or tissues (*24*). Electron tomography provides us the structural information at subcellular organization levels (*25*). The principles and methodology of electron tomography are similar to the ones of single-particle analysis (*3*), except here multiple images of the *same* specimen are recorded at many different angle. The typical steps of electron tomography are 1) put the prepared cryo-EM sample in the TEM; 2) tilt the samples typically in range +70º ~ -70º at 0.5º to 5º intervals and record an image at each step; then 3) translationally and rotationally align the raw data to produce the 3D reconstruction.

Electron Crystallography

Some biological macromolecules can form two-dimensional (2D) crystals, especially membrane proteins. In addition to 2D crystal, the electron crystallography technique also can be used to solve the structure of biomolecules with helical symmetry. For a particle whose structure is suitable to be solved by electron crystallography, it has translational symmetry in a plane. Electron diffraction will occur when electrons pass through the 2D crystal and the electron diffraction pattern is used to determine the amplitude. The phase is determined by the 2D images. The density of molecules is obtained via the inverse Fourier transform and, hence, the 3D reconstruction can be acquired. In 1990, electron crystallography was applied to solve protein structure – the structure of bacteriorhodopsin (*26*).

2.4 Fab Labeled Virus

Cryo-EM of antibody-labeled capsids provides a way to identify epitopes, e.g. (*27-30*). Virus is mixed with monoclonal or monospecific antibodies, and the resulting complexes are imaged followed by three-dimensional (3D) reconstruction of the complex. The use of antibody-binding fragments (Fabs) is preferred to avoid particle aggregation (from antibodies binding multiple particles) or to avoid large masses of disordered protein that may interfere with orientation finding (from antibodies binding to only one epitope). After successful 3D reconstruction of the complex, atomic coordinates of the antigen and Fab are fitted into the 3D density. (Usually coordinates of any Fab are sufficient.) By fitting antigen and antibody coordinates into the map, the epitope on the capsid surface can be identified (*30*).

We studied poliovirus cell-entry transition via three different monoclonal or monospecific antibodies to VP1, which bind to the residues 24-40, 39-55, or 93-103 of VP1. P1

Fab binds near the N-terminus, at residues 24-40 (see Chapter 3). C3 Fab binds a loop between the B and C β-strands (BC loop), residues 93-103 (*32*) (see Chapter 4). The last Fab I used binds residues 39-55 (*33, 34*) (see Chapter 5).

References

1. Brenner, S., and Horne, R. W. (1959) A negative staining method for high resolution electron microscopy of viruses, *Biochim Biophys Acta 34*, 103-110.

2. Adrian, M., Dubochet, J., Lepault, J., and McDowall, A. W. (1984) Cryo-electron microscopy of viruses, *Nature 308*, 32-36.

3. Steven, A., and Belnap, D. (2005) Electron microscopy and image processing: an essential tool for structural analysis of macromolecules, *Curr Protoc Protein Sci Chapter 17*, Unit 17 12.

4. Gonen, T., Cheng, Y., Sliz, P., Hiroaki, Y., Fujiyoshi, Y., Harrison, S. C., and Walz, T. (2005) Lipid-protein interactions in double-layered two-dimensional AQP0 crystals, *Nature 438*, 633-638.

5. Zhang, X., Jin, L., Fang, Q., Hui, W. H., and Zhou, Z. H. (2010) 3.3 A cryo-EM structure of a nonenveloped virus reveals a priming mechanism for cell entry, *Cell 141*, 472-482.

6. Henderson, R. (1995) The potential and limitations of neutrons, electrons and X-rays for atomic resolution microscopy of unstained biological molecules, *Q Rev Biophys 28*, 171-193.

7. Heymann, J. B., and Belnap, D. M. (2007) Bsoft: image processing and molecular modeling for electron microscopy, *J. Struct. Biol. 157*, 3-18.

8. Crowther, R. A., Amos, L. A., Finch, J. T., De Rosier, D. J., and Klug, A. (1970) Three dimensional reconstructions of spherical viruses by fourier synthesis from electron micrographs, *Nature 226*, 421-425.

9. Baker, T. S., and Cheng, R. H. (1996) A model-based approach for determining orientations of biological macromolecules imaged by cryoelectron microscopy, *J Struct Biol 116*, 120-130.

10. Sanz-García, E., Stewart, A. B., and Belnap, D. M. (2010) The random-model method enables *ab initio* three-dimensional reconstruction of asymmetric particles and determination of particle symmetry, *J. Struct. Biol. 171*, 216-222.

11. Ludtke, S. J., Baldwin, P. R., and Chiu, W. (1999) EMAN: semiautomated software for high-resolution single-particle reconstructions, *J Struct Biol 128*, 82-97.

12. Tang, G., Peng, L., Baldwin, P. R., Mann, D. S., Jiang, W., Rees, I., and Ludtke, S. J. (2007) EMAN2: an extensible image processing suite for electron microscopy, *J Struct Biol 157*, 38-46.

13. Frank, J., Radermacher, M., Penczek, P., Zhu, J., Li, Y., Ladjadj, M., and Leith, A. (1996) SPIDER and WEB: processing and visualization of images in 3D electron microscopy and related fields, *J Struct Biol 116*, 190-199.

14. Baxter, W. T., Leith, A., and Frank, J. (2007) SPIRE: the SPIDER reconstruction engine, *J Struct Biol 157*, 56-63.

15. Sorzano, C. O., Marabini, R., Velazquez-Muriel, J., Bilbao-Castro, J. R., Scheres, S. H., Carazo, J. M., and Pascual-Montano, A. (2004) XMIPP: a new generation of an open-source image processing package for electron microscopy, *J Struct Biol 148*, 194-204.

16. Yan, X., Sinkovits, R. S., and Baker, T. S. (2007) AUTO3DEM--an automated and high throughput program for image reconstruction of icosahedral particles, *J Struct Biol 157*, 73-82.

17. Grigorieff, N. (2007) FREALIGN: high-resolution refinement of single particle structures, *J Struct Biol 157*, 117-125.

18. van Heel, M., Harauz, G., Orlova, E. V., Schmidt, R., and Schatz, M. (1996) A new generation of the IMAGIC image processing system, *J Struct Biol 116*, 17-24.

19. Heymann, J. B., Chagoyen, M., and Belnap, D. M. (2005) Common conventions for interchange and archiving of three-dimensional electron microscopy information in structural biology, *J Struct Biol 151*, 196-207.

20. Vanhecke, D., Asano, S., Kochovski, Z., Fernandez-Busnadiego, R., Schrod, N., Baumeister, W., and Lucic, V. (2011) Cryo-electron tomography: methodology, developments and biological applications, *J Microsc 242*, 221-227.

21. Grunewald, K., Desai, P., Winkler, D. C., Heymann, J. B., Belnap, D. M., Baumeister, W., and Steven, A. C. (2003) Three-dimensional structure of herpes simplex virus from cryo-electron tomography, *Science 302*, 1396-1398.

22. Benjamin, J., Ganser-Pornillos, B. K., Tivol, W. F., Sundquist, W. I., and Jensen, G. J. (2005) Three-dimensional structure of HIV-1 virus-like particles by electron cryotomography, *J Mol Biol 346*, 577-588.

23. Fernandez-Busnadiego, R., Zuber, B., Maurer, U. E., Cyrklaff, M., Baumeister, W., and Lucic, V. (2010) Quantitative analysis of the native presynaptic cytomatrix by cryoelectron tomography, *J Cell Biol 188*, 145-156.

24. Medalia, O., Weber, I., Frangakis, A. S., Nicastro, D., Gerisch, G., and Baumeister, W. (2002) Macromolecular architecture in eukaryotic cells visualized by cryoelectron tomography, *Science 298*, 1209-1213.

25. Marco, S., Boudier, T., Messaoudi, C., and Rigaud, J. L. (2004) Electron tomography of biological samples, *Biochemistry (Mosc) 69*, 1219-1225.

26. Henderson, R., Baldwin, J. M., Ceska, T. A., Zemlin, F., Beckmann, E., and Downing, K. H. (1990) An atomic model for the structure of bacteriorhodopsin, *Biochem Soc Trans 18*, 844.

27. Wang, G. J., Porta, C., Chen, Z. G., Baker, T. S., and Johnson, J. E. (1992) Identification of a Fab interaction footprint site on an icosahedral virus by cryoelectron microscopy and X-ray crystallography, *Nature 355*, 275-278.

28. Trus, B. L., Newcomb, W. W., Booy, F. P., Brown, J. C., and Steven, A. C. (1992) Distinct monoclonal antibodies separately label the hexons or the pentons of herpes simplex virus capsid, *Proc Natl Acad Sci U S A 89*, 11508-11512.

29. Belnap, D. M., Watts, N. R., Conway, J. F., Cheng, N., Stahl, S. J., Wingfield, P. T., and Steven, A. C. (2003) Diversity of core antigen epitopes of hepatitis B virus, *Proc Natl Acad Sci U S A 100*, 10884-10889.

30. Conway, J. F., Watts, N. R., Belnap, D. M., Cheng, N., Stahl, S. J., Wingfield, P. T., and Steven, A. C. (2003) Characterization of a conformational epitope on hepatitis B virus core antigen and quasiequivalent variations in antibody binding, *J. Virol. 77*, 6466-6473.

31. Chow, M., Yabrov, R., Bittle, J., Hogle, J., and Baltimore, D. (1985) Synthetic peptides from four separate regions of the poliovirus type 1 capsid protein VP1 induce neutralizing antibodies, *Proc Natl Acad Sci U S A 82*, 910-914.

32. Wychowski, C., van der Werf, S., Siffert, O., Crainic, R., Bruneau, P., and Girard, M. (1983) A poliovirus type 1 neutralization epitope is located within amino acid residues 93 to 104 of viral capsid polypeptide VP1, *EMBO J 2*, 2019-2024.

33. Hovi, T., and Roivainen, M. (1993) Peptide antisera targeted to a conserved sequence in poliovirus capsid VP1 cross-react widely with members of the genus Enterovirus, *J Clin Microbiol 31*, 1083-1087.

34. Roivainen, M., Piirainen, L., Rysa, T., Narvanen, A., and Hovi, T. (1993) An immunodominant N-terminal region of VP1 protein of poliovirion that is buried in crystal structure can be exposed in solution, *Virology 195*, 762-765.

Chapter 3. An Externalized Polypeptide Partitions Between Two Distinct Sites

on Genome-Released Poliovirus Particles

3.1 Introduction

Poliovirus, the prototypic member of the picornavirus family, is one of the major model systems to study non-enveloped cell-entry mechanisms. Both the virus and its cellular receptor, poliovirus receptor (Pvr, also known as CD155), are extensively characterized and structurally defined (*1-8*). Like other picornaviruses, the poliovirus capsid is composed of 60 copies of four capsid proteins (VP1, VP2, VP3, and VP4), arranged with icosahedral symmetry (Fig. 1). VP1, VP2, and VP3 have a β-jellyroll topology and form prominent features known as the "mesa", "canyon", and "propeller" on the outer surface of the capsid (Fig. 1). VP4 lies in an extended conformation on the inner surface of the capsid, as do the N-terminal segments of VP1, VP2, and VP3. The capsid surrounds an approximately 7500-nucleotide, single-stranded RNA genome.

During cell entry, the binding of "native" virus (sedimentation coefficient 160S) to CD155 initiates conformational rearrangements that lead to formation of the genome-containing cell-entry intermediate (135S) particle (*1, 9, 10*). After uncoating (release of RNA into the host cell), the resultant empty capsid shell sediments at 80S.
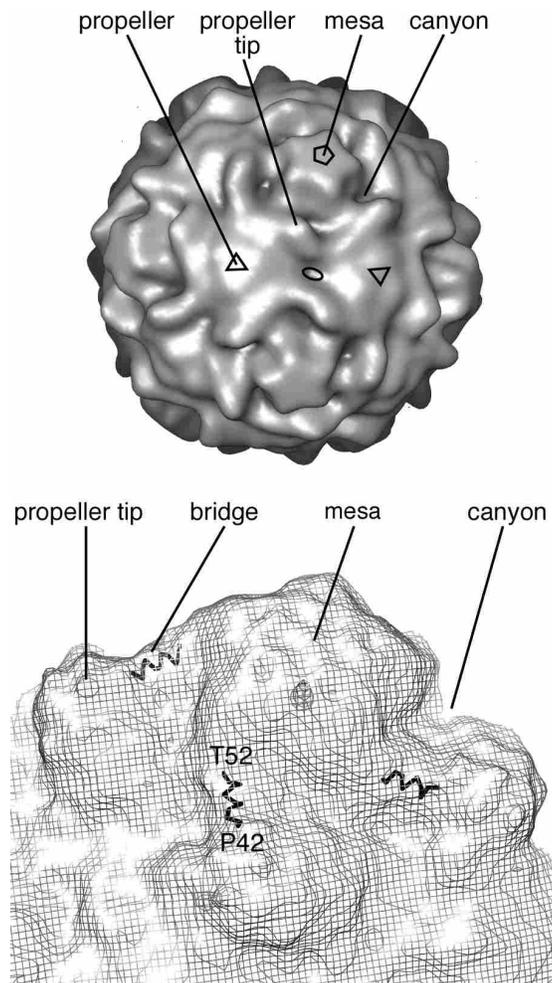
Figure 3.1 Structural features of 160S and 135S particles. (Top) Prominent structural features on the exterior of the 160S poliovirus particle (*5*). Fivefold (pentagon), threefold (triangle), and twofold (oval) symmetry axes are labeled. A second threefold axis is labeled to show an asymmetric unit—the triangle formed with the fivefold and two threefold axes as vertices. (The line connecting threefold axes passes through the twofold axis.) The asymmetric unit is the unique portion of the structure. The rest of the structure (59 other equivalent portions) is made by symmetry operations. (Bottom) Close-up view of four prominent structural features on the exterior of the 135S poliovirus particle (*13*), with one symmetry-related copy of "propeller tip" and "bridge" labeled. The predicted helices in the canyon are residues 42-52 from the N-terminus of VP1 (black wire diagram). The gray net is a cryo-EM reconstruction. For both 160S and 135S particles, the mesa is formed solely by VP1, the canyon and propeller by VP1, VP2, and VP3. The propeller tip is formed by the EF loop of VP2 and flanking polypeptide sequences from VP1 and VP3. Each mesa is centered on a fivefold symmetry axis, and each propeller is centered on a threefold symmetry axis.

The conformational rearrangements that form the 135S intermediate involve irreversible externalization of VP4 (which is myristoylated at its N-terminus (*11*)) and the N-terminal extension of VP1 (which is predicted to form an amphipathic helix (*12*)) from the capsid interior; externalization of these viral polypeptide sequences appears to facilitate poliovirus cell-entry (*5, 12-18*). These exposed sequences interact with—and in the case of the N-terminus of VP1 tether particles to—artificial membranes (*12, 19*). The exposed sequences also insert into cellular membranes during infection (*16*). Analyses of VP4 mutants show that VP4 plays a key role in the formation and properties of virus ion channels and in uncoating (*16*). For VP1, residues 1-53 were predicted to be exposed on the capsid surface, with residues 54-71 linking the externalized portion with the inner capsid surface; specifically, according to the model, the N-terminus of VP1 extends through a small opening between adjacent VP1 subunits, bridges the canyon, and emerges at the propeller tip (Fig. 1) (*13*). The N-terminal 31 residues were proposed to be mobile or disordered, but located near the propeller tip, far from the fivefold axis (*13*). Uncoating is accompanied by additional conformational changes in the virus particle that are reflected by the presence of at least three forms of the empty capsid, or 80S particle, (*20, 21*).

Cryogenic electron microscopy (cryo-EM) of antibody-labeled macromolecular complexes provides a way to map epitopes, (e.g. (*22-26*)). Antibodies are mixed with the complex, and the resulting combination is imaged followed by three-dimensional (3D) reconstruction. Monoclonal or monospecific antibodies are preferred because they provide specificity for the selected epitope, which gives consistency in the 3D reconstruction. The use of antigen-binding fragments (Fabs) is preferred to avoid formation of aggregates (e.g. immunoprecipitation) and to avoid large masses of disordered protein that add noise and interfere with orientation finding (from antibodies binding to only one epitope). After a 3D

reconstruction of the Fab-labeled complex is computed, atomic coordinates of the antigen and Fab are fitted into the 3D density. (Usually, coordinates of any Fab are sufficient.) In this way, an epitope can be localized on the surface of the complex. Conformational changes can be inferred if the epitope in question is exposed in one state but not another or if the epitope changes position.

To understand the structural rearrangements associated with the N-terminal residues of VP1, we determined 3D reconstructions from cryo-EM images of P1-Fab-labeled 135S and 80S particles. Polyclonal antibodies raised against peptide 1 (P1) recognize amino acid residues 24 to 40 of VP1 (*27*). The epitope monospecificity of these antibodies allows the location of the P1 epitope to be tracked as the virus particle undergoes the conformational rearrangements associated with cell entry and genome uncoating. We found that the P1 epitope is located on the propeller tip of the 135S particle, which is consistent with the previously modeled position of the N-terminus of VP1 (*13*). The P1 Fab binds to two sites on the 80S particle (one at the propeller tip, one at the twofold axis), and individual particles were found to have Fabs bound to one of the two sites or to both sites.

3.2 Materials and Methods

Preparation of viruses, 135S particles, 80S particles, and virus-Fab complexes.

Poliovirus virions (160S particles) were grown in a suspension of HeLa cells, harvested by centrifugation and freeze-thawing, and purified by CsCl density-gradient centrifugation as described previously (*9, 28*). Altered 135S particles were prepared via heat treatment (*9, 13*). Briefly, a solution of 160S particles was diluted fivefold in prewarmed low-salt buffer (20 mM Tris, 2 mM $CaCl_2$, pH 7.5) and was incubated at 50 ºC for 3 min. (sample placed in ice water

after incubation). P1 Fab was prepared from affinity-purified antisera raised against peptide P1 (*27*) by dialysis in 20 mM phosphate buffer and 10 mM EDTA (pH=7.0) and the ImmunoPure® Fab preparation kit (Pierce, Thermo Fisher Scientific, Rockford, Illinois, USA).

In our experiments we used heat to induce the change from native (160S) particle to cell-entry intermediate (135S) and RNA-released (80S) particles. 135S particles produced by heat or obtained from infected HeLa cells 1) infect cells normally non-permissive for poliovirus infection by 160S particles, 2) have lost VP4, 3) are similarly sensitive to proteolysis, and 4) similarly react with antibodies to the N-terminus of VP1 (*9*). 80S particles produced by heat share antigenicity, sedimentation properties, and protease sensitivity with empty particles that accumulate within cells and, like those particles, have externalized both VP4 and genomic RNA.

Solutions of 135S particles (0.6 mg/mL) and P1 Fab (0.8 mg/mL) were mixed at room temperature with an antibody-to-virus ratio of 600:1 (mole:mole). Thirty-four percent of the imaged particles in the 135S sample were 80S particles, cf. (*9*). 135S and 80S particles were readily distinguished by, respectively, the presence or absence of density corresponding to the viral RNA. These 80S particles were used to solve the structure of the 80S-P1 complex.

Electron Microscopy

Thin films containing poliovirus complexed with P1 Fabs were suspended over holey carbon films, vitrified, and imaged as described previously (*29*). A CM200 electron microscope (FEI, Hillsboro, Oregon, USA) equipped with Gatan 626 cryoholder (Pleasanton, California, USA) was used to record focal pairs of micrographs at magnifications of 38,000× at 120 kV.

3D reconstruction

Particle images were extracted, processed, and normalized as described (*5*). Focal settings

ranged from 0.81 to 2.24 μm underfocus. Focal-pair images were computationally combined for

orientation determination but used separately for origin determination and computation of the 3D

reconstruction. A previous reconstruction (*5*) or a model determined via common lines (*30*) was

used to begin iterative model-based determination of orientations and origins. Origins and

orientations of the extracted particles were determined via the model-based technique of *PFT2*

(*31*), which was adapted to use phase and amplitude information in orientation selection (*32*). 3D

reconstructions were calculated via *EM3DR2* (*30, 33*). Icosahedral symmetry was applied during

the reconstruction computations and orientation searches. Bsoft routines were used to assess and

correct for contrast transfer function (CTF) effects (*34*) via the algorithm by Conway and Steven

(*35*), but images within a focal pair were not combined during CTF correction. Spherically

averaged density plots were used to calibrate size (*34, 36*) against previously calibrated

structures (*5*) and a poliovirus X-ray crystal structure (*37*). 3D reconstructions were displayed at

contour levels designated by the number of standard deviations (σ) above the average map

density.

Classification of particles

Our initial 80S-P1 reconstruction showed two P1 Fab binding sites, and we sought to separate

particles by binding site. Using the UCSF Chimera package (*38*), we deleted Fabs via the

volume-eraser function, leaving structures with Fabs in only one type of site. The modified

maps served as the starting models for multiple-model-based classification, using a method

similar to that used by Heymann et al. (*39*). Each particle image was compared to a model

projection from each state. For a particle to be selected, a minimum correlation-coefficient value of 0.30 (for high- and low-pass Fourier filters of 90^{-1} Å^{-1} and 21^{-1}–16^{-1} Å^{-1}, respectively) was used as well as a minimum difference (range 0.005–0.010) between the correlation coefficients obtained from each form, i.e. a selected particle had to have a correlation-coefficient value of 0.30 or greater and be 0.005–0.010 higher than the value for the other 80S-P1 state. Fifty percent of the total number of particles were assigned to one of the two forms. By using the multiple-model-based classification method, we also attempted to classify the 80S particles into three groups: one with Fab bound at the propeller tip, one with Fab bound at the twofold axis, and one with Fab bound to both binding sites.

The Fab density in the 135S-P1 reconstruction was very low. We attribute this to a combination of low occupancy due to the relatively low affinity of the Fab for the 135S particle and to a reduction of density in the icosahedrally averaged reconstructions due to the flexibility of the epitope in the 135S particle (*13*). A 135S map (*5*) and the original 135S-P1 map were applied to classify the 135S particles, in the same manner as that used for the two forms of 80S-P1 (described in the previous paragraph). However, in this case, the classification values were used only to determine which particles from the previous (weak P1 Fab) set were used to compute the final reconstruction. Orientations and origins determined previously—without classification—were applied.

One-particle reconstruction

To assess Fab binding to individual particles, one-particle reconstructions (e.g. (*40*)) were computed to a limit of 40-Å resolution. (A close-to-focus and far-from-focus image pair was used to compute each "one-particle" reconstruction.) Icosahedral symmetry was applied during computation of the one-particle reconstructions, as it was in the multiple-particle reconstructions.

Central slices of these reconstructions were observed to assess whether Fabs were present and, if so, where the Fabs were bound.

Modeling

C3 Fab coordinates (*41*) were used to model the virus-P1 interaction. Coordinates were fitted "by-eye" into 135S-P1 and 80S-P1 maps via the UCSF Chimera package (*38*).

3.3 Results

We used antipeptide antibodies to the N-terminus of VP1 to locate this peptide in two key cell-entry intermediates. Purified virions were heated at 50°C to produce a mixture of 135S and 80S particles, and the particles were mixed with Fab fragments of a monospecific antibody raised against a peptide (P1) corresponding to residues 24-40 of VP1 (*27*).

Micrographs (i.e. same fields-of-view) contained complexes of the Fab with both 135S and 80S particles. These two particles were easily distinguished by the lack of internal density corresponding to the viral RNA in the 80S particles. The two forms were separated during particle image extraction ("boxing") and used to compute separate 3D reconstructions. Therefore, the imaging conditions for the 135S-P1 and 80S-P1 complexes are identical and are not responsible for the observed differences between the complexes.

We computed the 3D structures of the 135S-P1 and 80S-P1 complexes by cryo-EM and 3D image reconstruction (Table 1, Figs. 2-4). Estimates for the resolutions of the two structures based on Fourier shell coefficient analysis (using a 0.5 cutoff) were 12 Å for the 135S-P1 complex and 13 Å for the initial 80S-P1 complex (two other 80S-P1 reconstructions were calculated to 18-Å resolution, see section "Two P1 Fab binding positions in 80S-P1 complex"

below). The density corresponding to the Fab was weak in all reconstructions. However, continual density corresponding to the Fab extends outwards from the capsid with no evidence of a contrast fringe (e.g. the dark region immediately outside the capsid in Fig. 4A) that occurs at contrast edges in underfocused images at low resolution. For comparison, we note that a reconstruction of the virus-receptor complex, where the receptor is known to be bound at high occupancy, also has continuous density extending from the virus particle into the receptor (Fig. 4D). We therefore conclude that the Fab fragments are bound and that the weak density can be attributed to low occupancy, flexibility of the peptide epitope, overlapping monospecific Fabs, or a combination of these factors. To make Fab density easier to see, we also computed 3D reconstructions for both complexes at lower resolution (26Å for the 135S-P1 complex, 21Å for the initial 80S-P1 complex).

Because of conformational dynamics or "breathing", the N-terminus of VP1 (as well as VP4) is transiently and reversibly exposed in 160S particles, and this exposure is temperature dependent (*42, 43*). P1 Fab binding to 160S virions is, therefore, also temperature dependent—occurring to a significant extent at 37°C but not 25°C (*12, 27, 43*). In contrast, P1 antibody readily binds to 135S and 80S particles over a wide temperature range indicating the exposure and accessibility of this sequence on these particle surfaces (*12, 27*).

One P1 Fab binding position in 135S-P1 complex
On the 135S particle, P1 Fab binds to a single position within the asymmetric unit (Figs. 1, 2A-B). Fab density connects from the propeller tip outwards. In addition to having low occupancy (~16%, Fig. 4C), the reduced size of the Fab domains at this contour level (Fig. 2A,B) suggests that residues 24-40 of VP1 are flexible in the 135S particle or that monospecific Fabs bind to

slightly different amino acid residues (section "Fab occupancy and Fab epitope flexibility" in the

discussion explains factors contributing to the small size and low density of the Fabs).

Table 3.1 Microscopy and image reconstruction data

Sample	Particle images[a]	Resolu-tion[b] (Å)	EMDB ID
135S-P1	2110[c]	26[d]	5282
	10160[c]	12	5280
80S-P1 (both binding sites)	5256	21[d]	5284
		13	5283
80S-P1 (propeller tip only)	1132	18	5286
80S-P1 (twofold only)	1814	18	5285

[a]Total number of images, divide by two for the number of image pairs (focal pairs). These images were extracted

from seven focal-pair micrographs, where the first image in the pair was taken closer-to-focus and the second image

farther-from-focus. The pixel size for the reconstructions was 1.83 Å. For the orientation and origin determination,

images were only corrected for phase-flipping effects of the CTF. For the final, published reconstruction, images

were fully deconvoluted for CTF effects and a signal-decay correction was also applied (see Materials and Methods

section).

[b]Determined by the point at which the Fourier shell correlation (FSC) value reaches 0.5. For the FSC test, images

were only corrected for phase-flipping effects of the CTF.

[c]The difference in the number of particles used is attibutable to classification of particles that matched best with a

model containing an Fab on the propeller tip (2,110) against a model without an Fab bound (see Materials and

Methods). The other reconstruction (10,160) was from iterative model-based orientation and origin refinement

against all 135S particles in the data set. In the latter, all particles that matched well were included.

[d]Lower-resolution versions of the 12-Å 135S-P1 and 13-Å 80S-P1 maps were computed so that the bound Fabs

could be seen more easily.
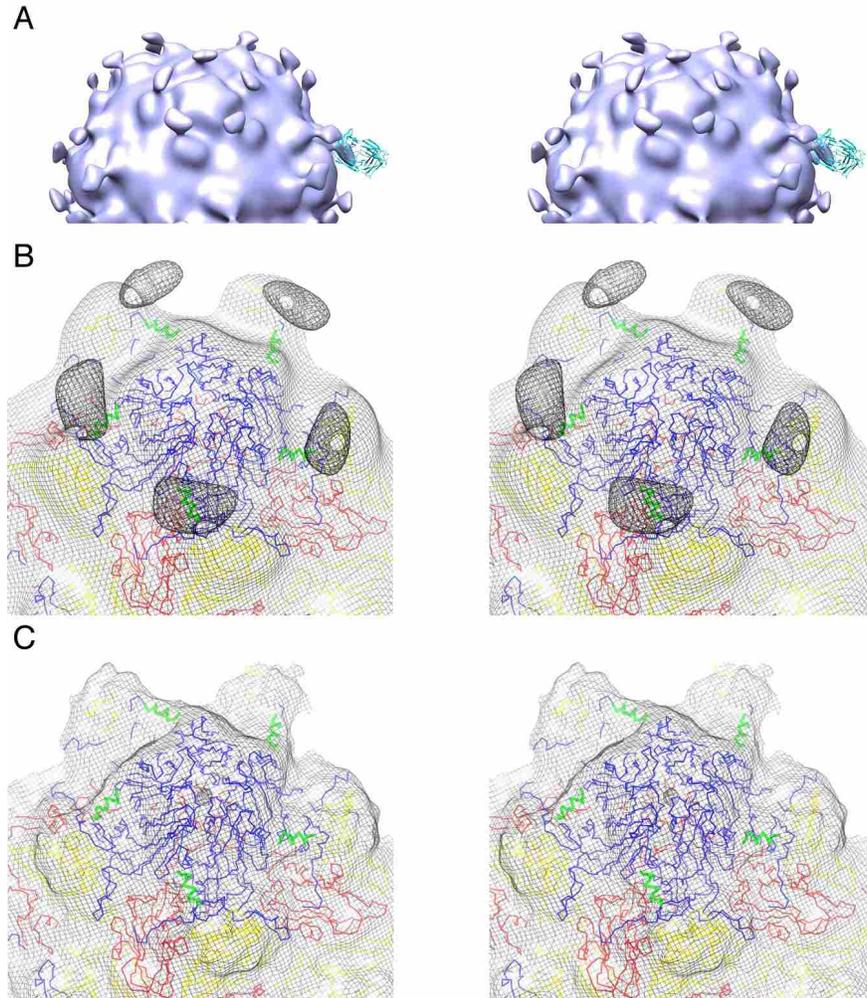
Figure 3.2 Stereo views of reconstructed 135S and 135S-P1 complex. (A) 135S-P1 complex (resolution 26 Å) reconstruction at a contour level of 0σ. Fab coordinates (cyan) are shown with the variable domain fitted into the P1 density. The fitting shown here is only to provide an estimate of the average Fab position. In the Fab variable domain, the volume occupied by the coordinates is significantly larger than the cryo-EM density, indicating that the epitope is flexible. (B,C) Coordinates (wire diagram) of the 135S model (*13*) (1XYR, Protein Data Bank) fitted in the 135S-P1 (B) and 135S (C) (*13*) maps (fine mesh). Coordinates for VP1 (blue), VP2 (yellow), VP3 (red) and residues 42-52 of the N-terminus of VP1 (green) are shown.
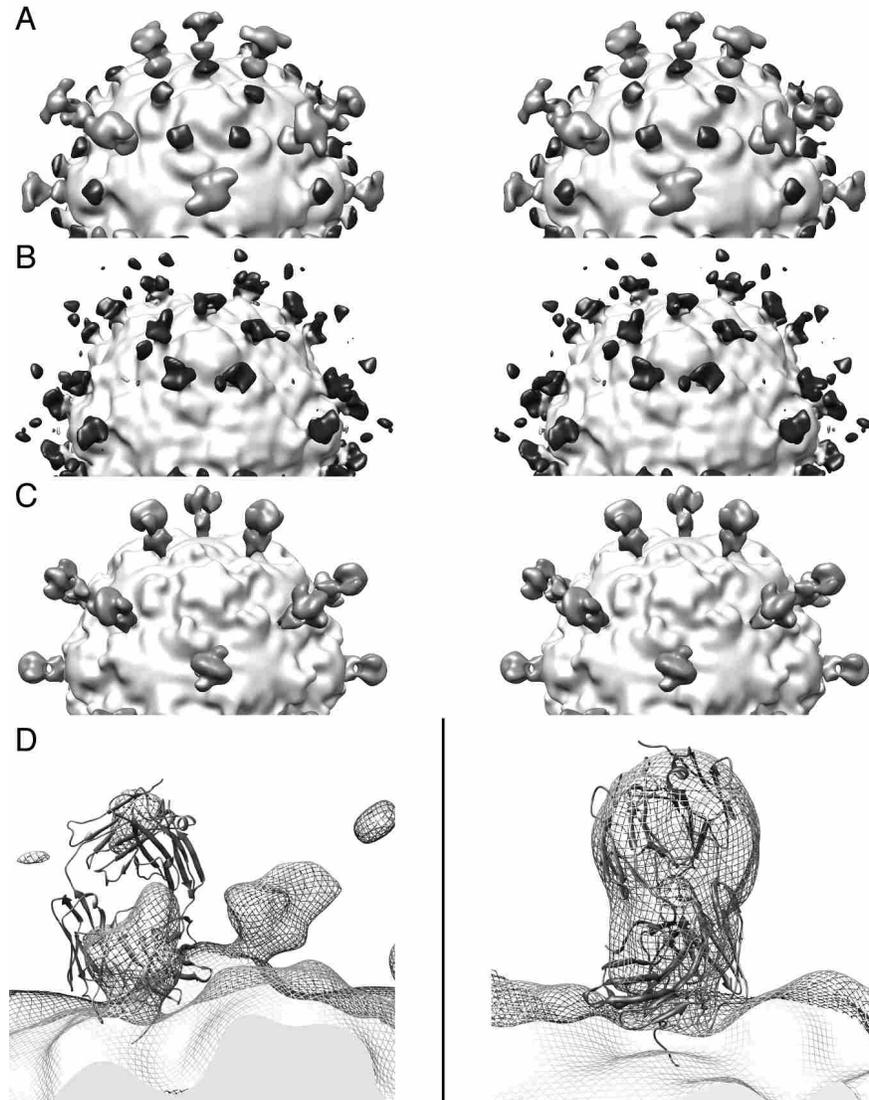
Figure 3.3 Views of reconstructed 80S-P1 complex. (A-C) Stereo views of 80S-P1 complex reconstructions. P1 Fabs bind 80S capsid (white) at the propeller tips (dark gray) and twofold axes (light gray). (A) The unclassified 80S-P1 (resolution 21 Å) reconstruction at a contour level of 0.2σ. (B,C) Reconstructions of 80S-P1 complexes (resolution 18 Å) with Fab bound to the propeller tip (B) and with Fab bound at the twofold axis (C), both at a contour level of 0.5σ. (D) Fab coordinates (ribbon structures) fitted into the two different binding sites in the 80S-P1 map (mesh). The Fab bound to the propeller tip is shown in the left panel. The Fab bound at the twofold axis is shown in the right panel. In both cases, the density in the antigen-binding domain (of the Fab) was not complete. The fitting shown here is only to provide an estimate of where the Fabs might be positioned. The constant (non-antigen binding) domain of the Fab bound at the twofold axis is larger than the volume occupied by the ribbon

model. The extra density likely results from twofold positioning of the epitope (but only one Fab can bind at a time), the monospecific nature of the antibody, or the flexibility of the constant domain.
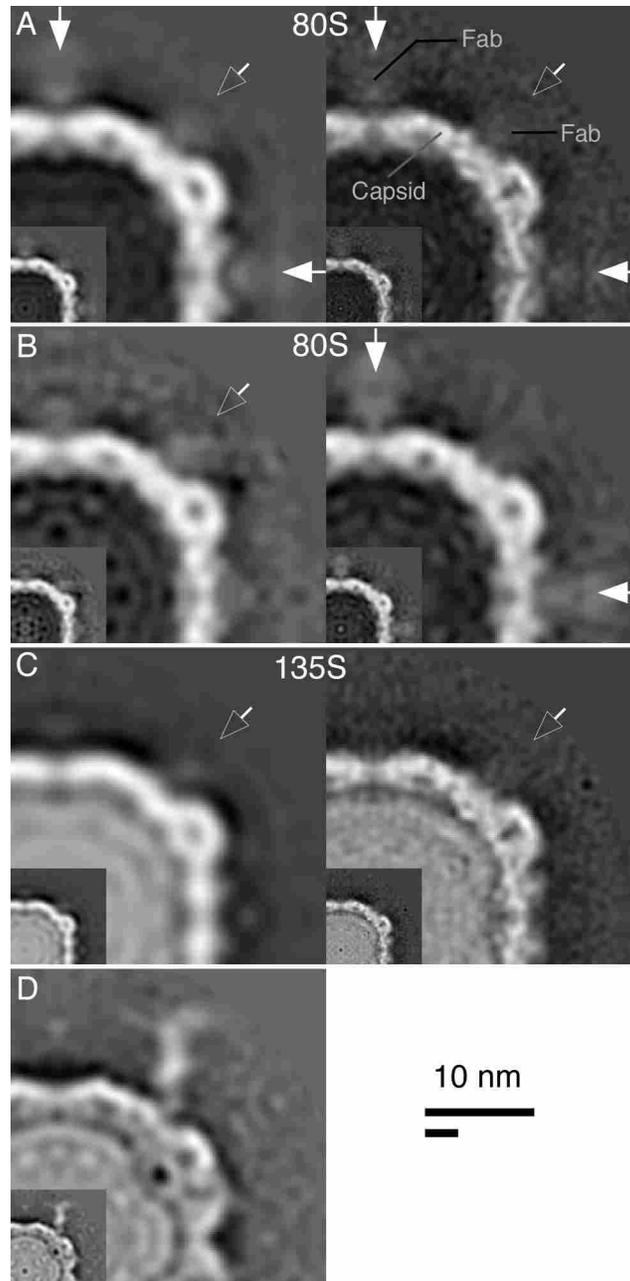
Figure 3.4 Binding of P1 Fab to poliovirus. Central slices from density maps of P1 Fab complexed with 80S particle (A,B) and 135S particle (C) and poliovirus (160S form) complexed with poliovirus receptor (Pvr) (*4*) (D). Highest densities are white. Arrows indicate P1 Fab-related density. Arrows indicate Fabs bound at the propeller tip (unfilled arrowhead) or twofold axis (filled arrowhead). The 80S-P1 complex maps were computed from

unclassified (A) and classified (B) particles. For (A); left, resolution 21 Å; right, resolution 13 Å. For (B); left, Fab bound to the propeller tip; right, Fab bound at the twofold axis, both structures at 18-Å resolution. For (C), 135S-P1: left, resolution 26 Å (from classified particles); right, resolution 12 Å (from unclassified particles). *Relative density estimates*: a sphere of radius 3 pixels was centered on the designated spots (A, right panel) and the average density computed. In the unclassified 80S-P1 map at resolution 21 Å (A, left), P1 Fab at the propeller tip (unfilled arrowhead) has 15% of capsid density and P1 Fab at the twofold axis (filled arrowhead) has 24%. In the classified 80S-P1 maps at resolution 18 Å (B), P1 Fab bound to the propeller tip (unfilled arrowhead) has 25% of capsid density (B, left), and P1 Fab bound at the twofold axis (filled arrowhead) has 23% (B, right). In the 135S-P1 map at resolution 21 Å (C, left), P1 Fab has 16% of capsid density. Insets, a smaller, unlabeled version of the figure, given to allow the faint Fab density to be seen more easily. (D) Control image showing Pvr attached to poliovirus 160S particle (*4*). Bars, longer bar for larger images, shorter bar for inset images. (Note: a faint bit of density appears on the twofold axes in panel B (left). This faint density does not appear in the surface rendering in Fig. 3B and therefore is much lower than the density observed at the propeller tip. We attribute this faint density to errors in classification and to artifacts that often appear along symmetry axes in reconstructions.)

Two P1 Fab binding positions in 80S-P1 complex

Inspection of the initial 80S-P1 map showed that P1 Fabs bound to two distinct areas on the capsid (Figs. 3A; 4A). The P1 Fab at the propeller tip in the 80S-P1 structure bound to the same site as in the 135S-P1 complex. A second Fab bound at the 80S-P1 twofold axis. We used classification methods to determine whether the two states were found on the same particles or if particles were in one state or the other.

We found that 80S-P1 particles with Fabs bound to the propeller tip or twofold axis could be separated by the position of the bound Fab (Fig. 3B-D, 4B). Therefore, the population of 80S-P1 particles exists in at least two states with the P1 epitope located at one of the two binding sites: the propeller tip (Figs. 3B; 3D,left; 4B,left) or the twofold axis (Figs. 3C; 3D,right; 4B,right). Although we cannot rule out that some "cross-contamination" in the propeller-tip and

twofold-axis data sets exists, the Fab density for each was clearly dominant in one form or the other (Fig. 3B,C).

In the particles with Fab at the twofold axes, the Fab-related density shows a direct connection to the twofold symmetry axes of the capsid (Fig. 3D). The density for the Fab at the twofold axes is twofold symmetric and is closer to the size of an Fab than is the density at the propeller tips of either the 135S-P1 or the 80S-P1 structures. Note, however, that the density for the constant domain is larger than needed, indicating either flexibility in the epitope being bound, overlapping monospecific antibodies, or that the two copies of the epitope at this site (which could be contributed by either of two twofold related copies of VP1) are oriented slightly differently.

To determine whether P1 epitopes can occupy simultaneously both locations on the same particle, we attempted to use correlation-based classification to separate the 80S-P1 particles into three classes: propeller-tip bound Fab, twofold-axis-bound Fab, and Fab bound to both. However, the number of Fabs bound per particle was relatively low (Fig. 4A,B), which gave little contribution from bound Fab in the noisy particle images and thus prevented clear discrimination among these three classes. (Note that the reconstruction showing Fabs bound to both sites (Figs. 3A, 4A) was an average structure of all selected 80S particles prior to classification.)

Because the classification experiment failed to give a conclusive answer, we decided to compute one-particle reconstructions. One-particle reconstructions are 3D reconstructions computed from *one* image of a particle. Although 3D reconstructions require multiple views of an object, one-particle reconstructions are possible for objects with icosahedral symmetry because one view has 59 other symmetry-related views. We computed one-particle

reconstructions to only 40-Å resolution because of the high noise level that arises from the limited averaging implicit in one-particle reconstructions. Several reconstructions showed Fabs bound to both the propeller tips and twofold axes of 80S particles (Fig. 5C). Other structures showed Fabs bound to either the propeller tips or twofold axes (Fig. 5A,B). Thus, these reconstructions demonstrated the existence of 80S particles where P1 epitopes are located at both the propeller tips and twofold axes simultaneously.
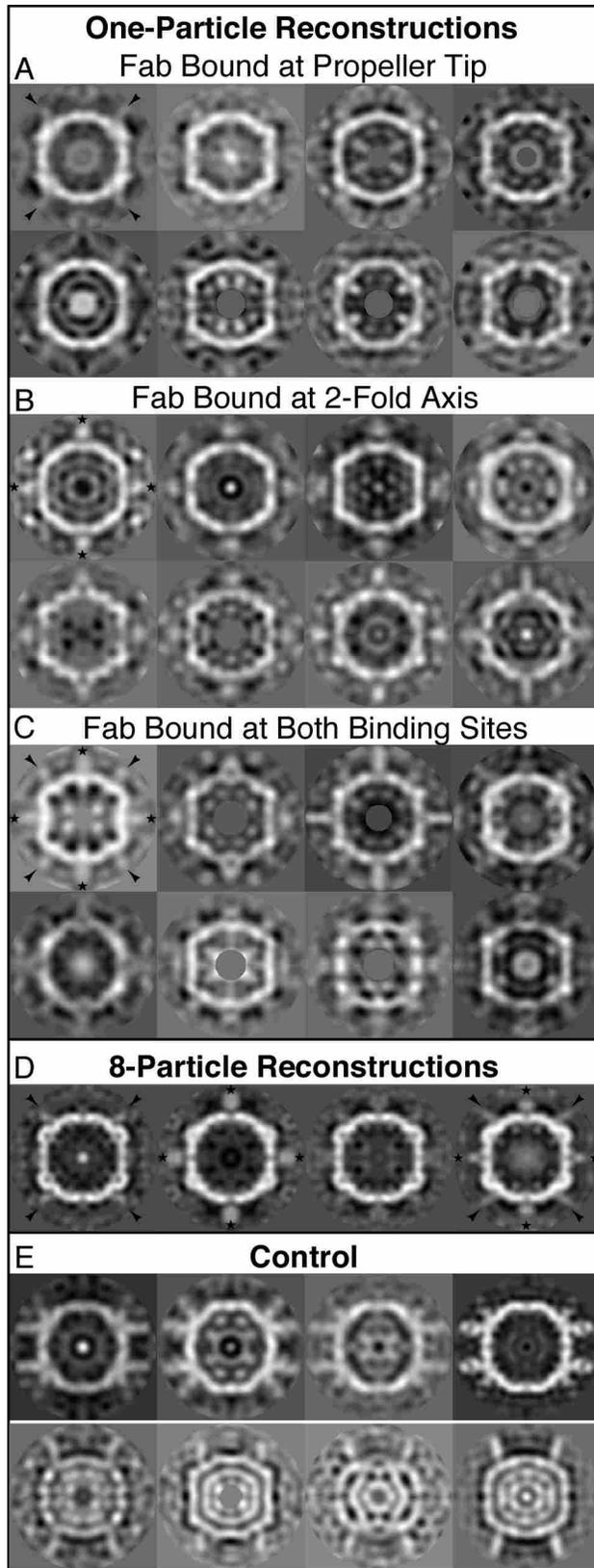
Figure 3.5 One- or Eight-Particle Reconstructions of 80S-P1 complexes. Arrows indicate Fab bound at the

propeller tip, and stars indicate Fab bound at the twofold axis. (A, B, C) Central slices of one-particle reconstructions of 80S-P1 complex with P1 Fab bound at the propeller tip (A), the twofold axis (B) and at both binding sites (propeller tip and twofold axis) (C). (D) Central slices of eight-particle reconstructions of 80S-P1. The same particle images that were used to make the one-particle reconstructions in A-C were combined to give the structures seen here. From left to right: eight-particle reconstruction of 80S-P1 with P1 Fab bound at the propeller tip; eight-particle reconstruction of 80S-P1 with P1 Fab bound at the twofold axis; mixed eight-particle reconstruction (four particles of 80S-P1 with P1 Fab bound at the propeller tip and four particles of 80S-P1 with P1 Fab bound at twofold axis); and eight-particle reconstruction of 80S-P1 with P1 Fab bound at both binding sites. E) Control structures. Central slices of one-particle reconstructions computed from a different poliovirus-antibody (C3) complex (top row) (J. Lin et al., unpublished) and the poliovirus-Pvr complex (bottom row) (*4*). The left three panels in each row are one-particle reconstructions and the rightmost panel is an eight-particle reconstruction. The one-particle reconstructions show bound Fab (top row) or bound receptor (bottom row). The C3 antibody binds very tightly to poliovirus 160S, 135S, and 80S particles (*12*) and Fabs were found to bind to the tips of the mesa (J. Lin et al., unpublished). Pvr binds to one side of the propeller tip and bridges the canyon (*4*). In A-E, the monotone gray circular center seen in some slices was added artificially to mask very high positive or negative density values at the center of the 3D reconstruction—a common artifact in one-particle, icosahedral reconstructions.

3.4 Discussion

In part because crystallization of picornavirus cell-entry intermediates has been unsuccessful, cryo-EM studies provide unique potential for structurally characterizing the entry process, e.g. (*4-8, 13, 20, 21, 44-48*). During viral entry, receptor-mediated conformational changes result in the externalization of the myristoylated protein VP4 and the N-terminal extension of VP1 (*12*), both of which become associated with membranes (*12, 16, 19*). In subsequent steps, unknown triggers result in the externalization of the viral RNA and its translocation across a membrane to gain access to the cytoplasm for replication (see (*1, 17, 18*)).

Because the externalized peptides are thought to play a role in internalization, genome release, and translocation of the genome across membranes (*1, 18*), a knowledge of the location of the externalized portion of VP1 is key to the refinement of models for the entry process. A previously published study of the 135S particle and a 135S particle in which the first 31 residues of VP1 were removed by proteolysis suggested that the N-terminus of VP1 is located at the propeller tip (*13*). Three-dimensional reconstructions of the 80S particle also suggested that the N-terminus of VP1 was located at the tips of the propeller in some but perhaps not all of the particles (*20*) (see section "N-terminus of VP1 makes conformational changes during uncoating" below). However, the 135S and 80S reconstructions lacked density for the N-terminus of VP1 (presumably because it is flexibly tethered to the virion). In this study, we took advantage of the availability of antibodies against the N-terminal extension of VP1 to probe its location in the 135S and 80S particles. The results are consistent with the results of the previous studies, but show that this peptide can be located in two different locations in the 80S particles. Surprisingly, these results also indicate that the same peptide in some cases can occupy two different positions in the same 80S particle, which represents a significant break from icosahedral symmetry for these particles.

Specificity of P1 Antibody

Evidence strongly suggests that the antibody raised against peptide P1 only recognizes amino acid residues 24 to 40 of VP1 and does not bind non-specifically to other regions of the 80S or 135S particles. Only one site is bound in 135S particles (Fig. 2A). In 80S particles, two sites are occupied, either one or the other or both (Figs. 3, 5). Anti-P1 sera only recognized the P1 peptide (VP1 residues 24-40), VP1, and the carrier protein to which the P1 peptide was attached; no

other peptides from VP1 were recognized, and VP2 and VP3 were unrecognized (*27*).

Recognition of anti-P1 sera was blocked by competition with P1 (*27*). Before its use in this

study, the antisera was affinity purified with the P1 peptide, thereby removing reactivity with the

carrier protein.

Fab occupancy and Fab epitope flexibility

Because 3D reconstructions of freestanding particles are averages of multiple particles that are

assumed to be similar, sub-volumes with lower average density must indicate lower occupancy,

flexible domains, or both. If the low-density sub-volume has the full shape of a protein domain,

then the domain must be rigidly positioned but have lower occupancy (i.e. not all positions in all

particles have the domain). If the lower density region is smaller or larger than the full shape of

the domain, then the domain must be flexible or have multiple rigid conformations. Overlapping

regions will have the highest densities. The higher the occupancy, the larger a flexible domain

will appear. Hence, observation of a small low-density portion of the Fab volume at the

propeller tip in 135S-P1 (Fig. 2A) or 80S-P1 (Figs. 3A-B;D,left) indicates not only low

occupancy, but that the P1 Fab at the propeller tip is located in multiple positions in the 135S and

80S particles.

If some parts of a structure have higher resolution than other parts, then the lower-

resolution is another indication of flexibility. We observed this pattern for the 135S-P1 and 80S-

P1 maps. Sections show a well-resolved capsid with fuzzy, poorly resolved density outside of

the capsid where Fab is bound (Fig. 4A,C, right panels). "Local" resolution tests (resolution of

small subvolumes of the reconstruction) confirmed the observation of higher resolution in the

capsid and lower resolution in the Fab regions (data not shown).

Each voxel (pixel volume) in a 3D reconstruction shows the average density (at the given xyz position) for the particles used. Therefore, density averages for flexible components will be more diffuse than for rigid components. Furthermore, the higher the resolution of a 3D map, the more unlikely flexible regions will be observed. If the 3D reconstruction is computed at lower resolution, flexible regions will be more apparent. This was the case with our 135S-P1 and 80S-P1 maps; Fab density was more easily observed at, respectively, 26- or 21-Å resolution than at 12- or 13-Å resolution (Fig. 4A,C). Even at the lower resolutions, Fab density was seen at relatively low contour levels in surface renderings (Figs. 2A-B; 3A) and faintly in density sections (Fig. 4A,C).

Continual density extending outwards from the capsid is additional evidence that Fabs are bound (Fig. 4). In many places, a dark region is located immediately outside the capsid density (e.g. Fig. 4A). This region is an effect of defocusing (specifically underfocusing) that is routinely performed during cryo-EM to enhance contrast. In incompletely corrected two-dimensional images and 3D image reconstructions, defocusing causes a fringe of intensity of opposite contrast at edges. No fringe is found at the Fab-binding sites, indicating the presence of continuous density. A similar connection was observed for receptor-bound particles (Fig. 4D).

Monoclonal vs. monospecific antibodies

An alternative reason for the appearance of flexible epitopes is that a monospecific, not monoclonal, antibody to residues 24-40 of VP1 was used. A monospecific (or polyclonal) antibody to this region could result in slight differences in binding among the Fabs bound. The average structure observed in the reconstructions would then have the appearance of a flexible epitope that had a monoclonal antibody bound.

For 3D cryo-EM reconstructions, monoclonal antibodies are usually preferred over monospecific antibodies because of the overlapping binding sites. Our observation of two binding sites in 80S particles suggests that monospecific antibodies—to a short peptide—may be valuable probes for assessing conformational changes. We do not know if the same amino acids bind to the monospecific antibody at the propeller-tip and twofold-axis epitopes. Even if the same amino acids are bound, the same Fab (with identical variable region) may not bind because the amino-acid conformation may differ. Therefore, a monoclonal antibody that binds to one conformation may not recognize the same amino acid residues after the conformational change. In this situation, one might erroneously conclude that the epitope was not exposed. Monospecific antibodies to short peptides may better recognize conformational differences and still provide enough specificity for structurally consistent 3D density maps. The appearance of a flexible epitope may always result from the use of monospecific antibodies.

N-terminus of VP1 is located near the propeller tip in 135S and 80S particles

The 3D reconstructions of 135S-P1 and 80S-P1 (Figs. 2A,B; 3A,B; 3D,left) show that P1 Fab binds to the propeller tip in 135S and 80S particles, with P1 Fab bound at the propeller tip alone or at both binding sites. These observations are consistent with existing models of 135S (*13*) and 80S (*20*) and with a difference map of 135S minus 135SΔN31 (*13*), which placed the P1 epitope (residues 24-40, (*27*)) near the propeller tip. For example, residues 42-52 of VP1 (modeled as an α-helix) are close to the propeller tip (Fig. 1,bottom; Fig. 2B,C) and difference density was observed at the propeller tip (*13*).

Non-synchronous changes in 80S particles

As in many other nonenveloped viruses, poliovirus capsid proteins are organized to form an icosahedrally symmetric shell. An important question in icosahedral virus assembly and disassembly is whether all copies of pertinent protein domains participate synchronously in the conformational changes associated with these processes and whether significant deviations from icosahedral symmetry can exist within an individual particle during conformational transitions. Because cryo-EM structures are averages of many particle images, structural features that are conveyed at lower resolution than the rest of the structure are likely caused by conformational variability among the population of particles. But, for symmetric particles such as poliovirus, these differences might be attributable to variations between particles that, individually, are symmetric. Here, we provide direct evidence that significant deviations from icosahedral symmetry—for portions of capsid proteins—do exist within the *same* particle. The observation of epitopes in two concurrent positions shows that significant portions of the capsid proteins within the icosahedral shell may have deviations from icosahedral symmetry and, hence, do not change conformation synchronously. Such deviations may be biologically significant during viral transitions.

80S-P1 particles with both Fab binding sites (Fig. 5C; 5D,right) show that the N-termini of VP1 are simultaneously located at two different sites (the propeller tips and twofold axes) on the same particle. This 80S state may indicate that during uncoating, the corresponding conformational change in the capsid is a gradual process. In other words, for an individual particle, the 60 copies of the N-terminus of VP1 are not required to change their conformations at the same time or in the same way.

As stated, the Fabs used in this experiment were monospecific, not monoclonal. Therefore, although P1 Fabs all bind within residues 24-40 of VP1, the Fabs bound at the propeller tips and twofold axes may recognize different amino-acid residues within the P1 epitope. However, the *straight-line* distance between antigen-binding sites on the propeller tip and the twofold axis is 52 (± 1) or 62 (± 0.4) Å, for the two closest twofold axes. (Measurement is based on placement of Fab coordinates into the Fab density, e.g. Fig. 3D). Assuming that 1) each residue occupies a linear distance of 3.8 Å along the polypeptide chain, 2) residues 24-40 are not in a straight-line conformation, and 3) each Fab binds several residues within the P1 peptide, P1 Fab binding to the propeller tips and twofold axes likely cannot result from two Fabs binding to different ends of the P1 epitope from one VP1 subunit. The seemingly simultaneous binding of P1 Fabs to different sites on the same 80S particle (in the icosahedrally averaged structure) most likely occurs because P1 epitopes from different VP1 subunits lie at a twofold axis or at a propeller tip.

We hypothesize that deviations from icosahedral symmetry are more likely to occur in extensions of the polypeptide chains (e.g. N-termini, C-termini, or large loops) that are not critical to interactions within the core shell structure. For example, the 53-residue N-terminus of VP1 could lie in different conformations on the capsid surface without necessarily disturbing interactions between the β-jellyroll cores of VP1, VP2, and VP3, which form the shell. If interactions of cores in one portion of the capsid are altered, we hypothesize that these changes would be more likely to propagate rapidly throughout the capsid shell. In our case, the symmetry-averaged cores of the VP1-3 subunits were resolved at 13-Å or better, indicating that the core structures of 80S particles were well ordered.

N-terminus of VP1 makes conformational changes during uncoating

The transition of VP1 residues 24-40 from the propeller tip to the twofold axis appears to be part of uncoating. Besides having the same binding site as in the 135S-P1 complex, P1 Fabs bind to a second site in 80S-P1—at the twofold axis—indicating either that conformational rearrangements occur during uncoating or that an additional variable, characteristic of the multiple-form 80S particle (*20, 21*), exists. Because only one P1 Fab at a time can bind to residues 24-40 of VP1 (see previous section), our results show that 80S particles contain the epitope in one or both of two locations.

The observation that peptide 1 (P1) changes position and perhaps conformation during the 135S-to-80S transition is consistent with previously published immunoprecipitation experiments that showed a change in the N-terminus of VP1 between these two states. Titers of P1 monospecific and monoclonal antibodies and a monospecific antibody against peptide 0 (P0, residues 7-24) for 80S particles differed significantly from the corresponding titers for 135S particles (*12*). The transition from the 135S particle to the 80S particle also involves the externalization of the RNA genome of the particle, and, interestingly, the new position for the P1 peptide is very close to the position where RNA was shown to be released from the particle (*21*)—suggesting that the movement of the peptide may play a role in RNA release (often referred to as "uncoating") during infection.

Previous studies have shown at least three distinct forms of heat-derived 80S particles (*20, 21*). In these studies, the 80S particles from preparations heated at 56 ºC for shorter times had increased numbers of particles in the conformation labeled the "early" form (80S.e). Conversely, samples heated for longer times showed increased numbers of the "late" form (80S.l). Because both 80S.e and 80S.l were seen by Levy et al. (*20*) at all time points, even their

4 min. incubation, the 80S particles in this study are also likely in these two states. Our sample was prepared at a lower temperature (50 ºC) for a relatively short time (3 min.). These conditions are typically used to produce 135S particles, but even this mild treatment typically produces a significant number of 80S particles (*9*).

We compared the 80S.e and 80S.l maps (*20*) to our 80S structures but were unable to make satisfactory distinctions, i.e. the correlation coefficients were nearly identical. Nevertheless, Levy et al. (*20*) showed differences between 80S.e and 80S.l in a density feature that is ascribed to a predicted helix spanning residues 41-53 from VP1 in the 135S structure (*13*). If this sequence assignment is accurate, it would place the residues corresponding to the P1 epitope at the tip of the propeller, as observed in this (Figs. 2,3) and a previous (*13*) study. Density for the helix is weaker in the 80S.e reconstruction than helix density in the 80S.l or 135S reconstructions, implying that some fraction of the helices (and perhaps the P1 epitopes as well) have moved in the 80S.e particles. The moved segments may be located at the twofold axes and, therefore, are responsible for the Fab binding at the twofold axes that we observed. Both 80S.e and 80S.l reconstructions had holes in the shell that suggested the viral RNA may be released near a twofold axis (*20*). A third 80S intermediate actually showed RNA leaving the capsid near the twofold axis at a site that corresponded to these holes (*21*). Because our experiment was carried out under different conditions from those used by Levy et al. (*20*), we cannot rule out the possibility that our results represent additional conformations of 80S particles not seen in the previous studies (*20, 21*).

Canyon-exit model

During cell entry, native poliovirus (160S) binds to its receptor, which stimulates conversion to the 135S cell-entry intermediate particle (*12*). During this transition, the membrane-binding entities, VP4 and the N-terminus of VP1, are externalized. Externalization of these proteins requires conformational adjustments in the capsid. Based on hypothesized parallels between the uncoating processes of human rhinoviruses and poliovirus, one model proposes that receptor binding induces formation of a channel along the fivefold axes, and that VP4 and the N-terminus of VP1 exit the capsid through this channel (*44, 48, 49*). In an alternative (canyon-exit) model, VP4 and the N-terminus of VP1 exit the capsid at the base of the canyon (*5, 13*). Our structures of virus-antibody complexes are consistent with the latter model.

The 135S-P1 reconstruction reported here supports the "canyon-exit" model by providing more evidence that at least a portion of the externalized N-terminus of VP1 locates at the propeller tip. The alpha helix proposed for residues 42 to 52 of VP1 is very close to the P1 Fab binding site at the propeller tip, close to the canyon and the threefold axis (Fig. 1 and Fig. 2B), which is consistent with the P1 epitope (residues 24-40) being located nearby and, hence, that the N-terminus of VP1 is at the propeller tip, as modeled by Bubeck et al. (*13*) for 135S particles. Our results are also consistent with a difference-density map, between V8-protease-cleaved 135S and unmodified 135S particles, that showed difference-density at the tip of the propeller (*13*).

P1 Fab was also bound at the propeller tip in 80S-P1 particles. This is consistent with the model of the 80S structure by Levy et al. (*20*). The Fab density bound at the propeller tip was highest near the propeller tip (Fig. 2A-B; 3A-B,D,left), indicating that P1 Fab was most constrained where it is bound to the capsid. The density volume of P1 Fab bound at the propeller tip is smaller than that of the P1 Fab bound at the twofold axis (Fig. 2A-B; 3), which indicates

the N-terminus of VP1 has more flexibility at the propeller tip than at the twofold axis. The increased flexibility at the propeller tip may be necessary for the N-terminus of VP1 to become imbedded in the membrane to prepare the virus for uncoating. The more rigid twofold-axis position may be required for or be a consequence of RNA release.

References

1. Hogle, J. M. (2002) Poliovirus cell entry: common structural themes in viral cell entry pathways, *Annual Reviews of Microbiology 56*, 677-702.

2. Hogle, J. M., Chow, M., and Filman, D. J. (1985) Three-dimensional structure of poliovirus at 2.9 Å resolution, *Science 229*, 1358-1365.

3. Filman, D. J., Syed, R., Chow, M., Macadam, A. J., Minor, P. D., and Hogle, J. M. (1989) Structural factors that control conformational transitions and serotype specificity in type 3 poliovirus, *EMBO J 8*, 1567-1579.

4. Belnap, D. M., McDermott, B. M., Jr., Filman, D. J., Cheng, N., Trus, B. L., Zuccola, H. J., Racaniello, V. R., Hogle, J. M., and Steven, A. C. (2000) Three-dimensional structure of poliovirus receptor bound to poliovirus, *Proc. Natl. Acad. Sci. USA 97*, 73-78.

5. Belnap, D. M., Filman, D. J., Trus, B. L., Cheng, N., Booy, F. P., Conway, J. F., Curry, S., Hiremath, C. N., Tsang, S. K., Steven, A. C., and Hogle, J. M. (2000) Molecular tectonic model of virus structural transitions: the putative cell entry states of poliovirus, *J. Virol. 74*, 1342-1354.

6. He, Y. N., Bowman, V. D., Mueller, S., Bator, C. M., Bella, J., Peng, X. H., Baker, T. S., Wimmer, E., Kuhn, R. J., and Rossmann, M. G. (2000) Interaction of the poliovirus receptor

with poliovirus, *Proceedings of the National Academy of Sciences of the United States of America 97*, 79-84.

7. Xing, L., Tjarnlund, K., Lindqvist, B., Kaplan, G. G., Feigelstock, D., Cheng, R. H., and Casasnovas, J. M. (2000) Distinct cellular receptor interactions in poliovirus and rhinoviruses, *EMBO Journal 19*, 1207-1216.

8. Zhang, P., Mueller, S., Morais, M. C., Bator, C. M., Bowman, V. D., Hafenstein, S., Wimmer, E., and Rossmann, M. G. (2008) Crystal structure of CD155 and electron microscopic studies of its complexes with polioviruses, *Proc. Natl. Acad. Sci. USA 105*, 18284-18289.

9. Curry, S., Chow, M., and Hogle, J. M. (1996) The poliovirus 135S particle is infectious, *J. Virol. 70*, 7125-7131.

10. Huang, Y., Hogle, J. M., and Chow, M. (2000) Is the 135S poliovirus particle an intermediate during cell entry?, *J. Virol. 74*, 8757-8761.

11. Chow, M., Newman, J. F., Filman, D., Hogle, J. M., Rowlands, D. J., and Brown, F. (1987) Myristylation of picornavirus capsid protein VP4 and its structural significance, *Nature 327*, 482-486.

12. Fricks, C. E., and Hogle, J. M. (1990) Cell-induced conformational change in poliovirus: externalization of the amino terminus of VP1 is responsible for liposome binding, *J. Virol. 64*, 1934-1945.

13. Bubeck, D., Filman, D. J., Cheng, N., Steven, A. C., Hogle, J. M., and Belnap, D. M. (2005) The structure of the poliovirus 135S cell entry intermediate at 10-Angstrom resolution reveals the location of an externalized polypeptide that binds to membranes, *J. Virol. 79*, 7745-7755.

14. Hogle, J. M., and Racaniello, V. R. (2002) *Poliovirus Receptors and Cell Entry*, ASM Press, Washington, D. C.

15. Brandenburg, B., Lee, L. Y., Lakadamyali, M., Rust, M. J., Zhuang, X., and Hogle, J. M. (2007) Imaging poliovirus entry in live cells, *PLoS Biol 5*, e183.

16. Danthi, P., Tosteson, M., Li, Q.-h., and Chow, M. (2003) Genome delivery and ion channel properties are altered in VP4 mutants of poliovirus, *J. Virol. 77*, 5266-5274.

17. Tuthill, T. J., Groppelli, E., Hogle, J. M., and Rowlands, D. J. (2010) Picornaviruses, *Curr Top Microbiol Immunol 343*, 43-89.

18. Levy, H., Bostina, M., Filman, D. J., and Hogle, J. M. (2010) Cell Entry: A Biochemical and Structural Perspective, In *The Picornaviruses* (Ehrenfeld, E., Domingo, E., and Roos, R. P., Eds.), pp 87-104, ASM Press, Washington, DC.

19. Tuthill, T. J., Bubeck, D., Rowlands, D. J., and Hogle, J. M. (2006) Characterization of early steps in the poliovirus infection process: receptor-decorated liposomes induce conversion of the virus to membrane-anchored entry-intermediate particles, *J Virol 80*, 172-180.

20. Levy, H. C., Bostina, M., Filman, D. J., and Hogle, J. M. (2010) Catching a virus in the act of RNA release: a novel poliovirus uncoating intermediate characterized by cryo-electron microscopy, *J Virol 84*, 4426-4441.

21. Bostina, M., Levy, H., Filman, D. J., and Hogle, J. M. (2011) Poliovirus RNA is released from the capsid near a twofold symmetry axis, *J. Virol. 85*, 776-783.

22. Wang, G. J., Porta, C., Chen, Z. G., Baker, T. S., and Johnson, J. E. (1992) Identification of a Fab interaction footprint site on an icosahedral virus by cryoelectron microscopy and X-ray crystallography, *Nature 355*, 275-278.

23. Trus, B. L., Newcomb, W. W., Booy, F. P., Brown, J. C., and Steven, A. C. (1992) Distinct Monoclonal-Antibodies Separately Label the Hexons or the Pentons of Herpes-Simplex Virus Capsid, *Proceedings of the National Academy of Sciences of the United States of America 89*, 11508-11512.

24. Jiang, Q.-X., Wang, D.-N., and MacKinnon, R. (2004) Electron microscopic analysis of KvAP voltage-dependent K^+ channels in an open conformation, *Nature 430*, 806-810.

25. Belnap, D. M., Watts, N. R., Conway, J. F., Cheng, N., Stahl, S. J., Wingfield, P. T., and Steven, A. C. (2003) Diversity of core antigen epitopes of hepatitis B virus, *Proceedings of the National Academy of Sciences of the United States of America 100*, 10884-10889.

26. Conway, J. F., Watts, N. R., Belnap, D. M., Cheng, N., Stahl, S. J., Wingfield, P. T., and Steven, A. C. (2003) Characterization of a conformational epitope on hepatitis B virus core antigen and quasiequivalent variations in antibody binding, *Journal of Virology 77*, 6466-6473.

27. Chow, M., Yabrov, R., Bittle, J., Hogle, J., and Baltimore, D. (1985) Synthetic peptides from four separate regions of the poliovirus type 1 capsid protein VP1 induce neutralizing antibodies, *Proc Natl Acad Sci U S A 82*, 910-914.

28. Rueckert, R. R., and Pallansch, M. A. (1981) Preparation and characterization of encephalomyocarditis (EMC) virus, In *Interferons* (Pestka, S., Ed.), pp 315-325, Academic Press, New York.

29. Zlotnick, A., Cheng, N., Conway, J. F., Booy, F. P., Steven, A. C., Stahl, S. J., and Wingfield, P. T. (1996) Dimorphism of Hepatitis B Virus Capsids Is Strongly Influenced by the C-Terminus of the Capsid Protein, *Biochemistry 35*, 7412-7421.

30. Fuller, S. D., Butcher, S. J., Cheng, R. H., and Baker, T. S. (1996) Three-dimensional reconstruction of icosahedral particles--the uncommon line, *J. Struct. Biol. 116*, 48-55.

31. Baker, T. S., and Cheng, R. H. (1996) A model-based approach for determining orientations of biological macromolecules imaged by cryo-electron microscopy, *J. Struct. Biol. 116*, 120-130.

32. Sanz-García, E., Stewart, A. B., and Belnap, D. M. (2010) The random-model method enables *ab initio* three-dimensional reconstruction of asymmetric particles and determination of particle symmetry, *J. Struct. Biol. 171*, 216-222.

33. Crowther, R. A., Amos, L. A., Finch, J. T., DeRosier, D. J., and Klug, A. (1970) Three Dimensional Reconstructions of Spherical Viruses by Fourier Synthesis from Electron Micrographs, *Nature 226*, 421-425.

34. Heymann, J. B., and Belnap, D. M. (2007) Bsoft: image processing and molecular modeling for electron microscopy, *J. Struct. Biol. 157*, 3-18.

35. Conway, J. F., and Steven, A. C. (1999) Methods for reconstructing density maps of 'single' particles from cryoelectron micrographs to subnanometer resolution, *J. Struct. Biol. 128*, 106-118.

36. Belnap, D. M., Grochulski, W. D., Olson, N. H., and Baker, T. S. (1993) Use of radial density plots to calibrate image magnification for frozen-hydrated specimens, *Ultramicroscopy 48*, 347-358.

37. Wien, M. W., Curry, S., Filman, D. J., and Hogle, J. M. (1997) Structural studies of poliovirus mutants that overcome receptor defects, *Nature Struct. Biol. 4*, 666-674.

38. Pettersen, E. F., Goddard, T. D., Huang, C. C., Couch, G. S., Greenblatt, D. M., Meng, E. C., and Ferrin, T. E. (2004) UCSF chimera - A visualization system for exploratory research and analysis, *Journal of Computational Chemistry 25*, 1605-1612.

39. Heymann, J. B., Conway, J. F., and Steven, A. C. (2004) Molecular dynamics of protein complexes from four-dimensional cryo-electron microscopy, *J. Struct. Biol. 147*, 291-301.

40. Castón, J. R., Belnap, D. M., Steven, A. C., and Trus, B. L. (1999) A strategy for determining the orientations of refractory particles for reconstruction from cryo-electron micrographs with particular reference to round, smooth-surfaced, icosahedral viruses, *J. Struct. Biol. 125*, 209-215.

41. Wien, M. W., Filman, D. J., Stura, E. A., Guillot, S., Delpeyroux, F., Crainic, R., and Hogle, J. M. (1995) Structure of the complex between the Fab fragment of a neutralizing antibody for type 1 poliovirus and its viral epitope, *Nature Struct. Biol. 2*, 232-243.

42. Roivainen, M., Piirainen, L., Rysä, T., Närvänen, A., and Hovi, T. (1993) An immunodominant N-terminal region of VP1 protein of poliovirion that is buried in crystal structure can be exposed in solution, *Virology 195*, 762-765.

43. Li, Q., Gomez Yafal, A., Lee, Y. M.-H., Hogle, J., and Chow, M. (1994) Poliovirus neutralization by antibodies to internal epitopes of VP4 and VP1 results from reversible exposure of these sequences at physiological temperature, *J. Virol. 68*, 3965-3970.

44. Hewat, E. A., and Blaas, D. (2004) Cryoelectron microscopy analysis of the structural changes associated with human rhinovirus type 14 uncoating, *J Virol 78*, 2935-2942.

45. Hewat, E. A., Neumann, E., and Blaas, D. (2002) The concerted conformational changes during human rhinovirus 2 uncoating, *Molecular Cell 10*, 317-326.

46. Hewat, E. A., Neumann, E., Conway, J. F., Moser, R., Ronacher, B., Marlovits, T. C., and Blaas, D. (2000) The cellular receptor to human rhinovirus 2 binds around the 5-fold axis and not in the canyon: a structural view, *EMBO J. 19*, 6317-6325.

47. Neumann, E., Moser, R., Snyers, L., Blaas, D., and Hewat, E. A. (2003) A cellular receptor of human rhinovirus type 2, the very-low-density lipoprotein receptor, binds to two neighboring proteins of the viral capsid, *J. Virol. 77*, 8504-8511.

48. Kolatkar, P. R., Bella, J., Olson, N. H., Bator, C. M., Baker, T. S., and Rossmann, M. G. (1999) Structural studies of two rhinovirus serotypes complexed with fragments of their cellular receptor, *EMBO J 18*, 6249-6259.

49. Giranda, V. L., Heinz, B. A., Oliveira, M. A., Minor, I., Kim, K. H., Kolatkar, P. R., Rossmann, M. G., and Rueckert, R. R. (1992) Acid-induced structural changes in human rhinovirus 14: possible role in uncoating, *Proc Natl Acad Sci U S A 89*, 10213-10217.

Chapter 4. Flexibility of the BC loop of the Poliovirus Capsid Protein VP1

During Cell Entry

4.1 Introduction

The poliovirus capsid is composed of 60 copies each of four capsid proteins (VP1, VP2, VP3, and VP4), arranged with icosahedral symmetry (Fig. 4.1), surrounding an approximately 7500-nucleotide, single-stranded RNA genome. VP4 and the amino-terminal segments of VP1, VP2, and VP3 lie on the inner surface of the capsid with extended conformations. The external surface of the capsid is constituted of VP1, VP2, and VP3.
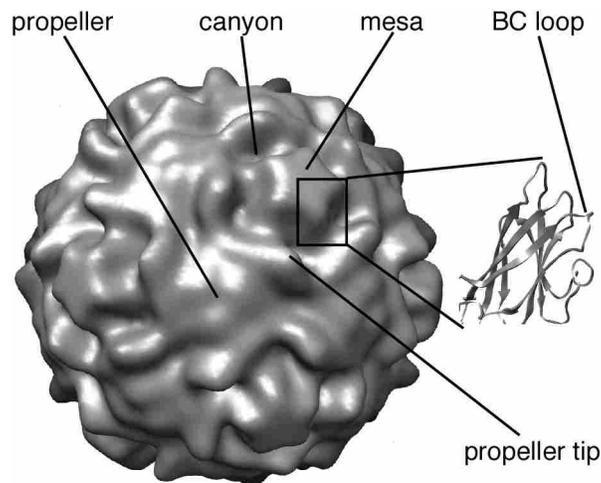
Figure 4.1 Structural features of 160S particle. Prominent structural features on the exterior of the 160S poliovirus particle (*1*), with an expanded representation showing the core β-jellyroll subunit and BC loop of VP1 (*2*) at a tip of the star-shaped "mesa".

During cell-entry, poliovirus (sedimentation coefficient, 160S) binds to its receptor, CD155, which initiates conformational rearrangements and forms the cell-entry intermediate (135S) particle. After RNA is released into the host cell, the empty poliovirus capsid sediments

at 80S. The conformational rearrangements during the 160S-to-135S transition involve irreversible externalization of VP4 and the N-terminal domain of VP1 (*3-5*). Poliovirus is an excellent model system to study cell-entry mechanisms of non-enveloped viruses (*6*). Studies of these conformational changes will aid understanding of cell entry of picornaviruses and perhaps of other non-enveloped viruses (*7, 8*).

A loop connecting the B and C β-strands of the VP1 β-jellyroll ("BC loop") is located at each tip of the star-shaped mesa surrounding the particle fivefold axes (Fig. 4.1). As shown by several studies, this loop (residues 93-103) is a major antibody-neutralizing site (*9-16*). One of the neutralizing antibodies that recognize this loop is the C3 monoclonal antibody, which was generated by immunizing mice with 80S poliovirus particles (*10*). This monoclonal antibody binds 160S, 135S, and 80S particles (*3*).

A crystal structure of the Fab fragment of this antibody with a peptide corresponding to residues 93-103 has been reported (*17*). The structure of the peptide in the complex differs significantly from the structure of the peptide in the BC loop of the 160S particle, suggesting that the loop is sufficently flexible to change structure upon antibody binding. This observation suggests the question of whether the same phenomenon occurs when the antibody binds in an assembled particle.

With the exception of the 160S particle (*2, 18, 19*), atomic-resolution structures of poliovirus cell-entry intermediates have been elusive, and fitting of atomic structures into density maps produced by cryogenic electron microscopy (cryo-EM) has been the only method to approach the goal of understanding poliovirus transitions at near-atomic detail.

To track the location of the BC loop in the three cell-entry states, we mixed the Fab fragment of the monoclonal C3 antibody with 160S, 135S, and 80S particles, and structures of

the respective complexes were solved by cryo-EM. The resulting structures of 160S-C3, 135S-C3 and 80S-C3 particles showed that the BC loop changes radius significantly (~ 7 Å) and twists slightly (15°) during the 160S-to-135S transition, with little further change in the 135S-to-80S transition. The locations of C3 in the 160S-C3, 135S-C3 and 80S-C3 maps are consistent with the positions of the BC loop in X-ray crystal structures of 160S particles (*2, 18, 19*) and in pseudo-atomic models of the 135S (*1, 4*) and 80S (*20*) particles. Our results suggest that the conformation of the BC loop is affected by antibody binding.

4.2 Materials and Methods

Preparation of viral and Fab complex.

Poliovirus virions (160S particles) and C3 Fab were prepared as described previously (*17, 21, 22*). Altered 135S particles were prepared via heat treatment (50 ºC for 3 min.) of 160S particles in low-salt buffer containing 2 mM $CaCl_2$, as described previously (*4, 22*). Equal volumes of 160S-particle (3.9 mg/ml) and C3-Fab (1.7 mg/ml) solutions were mixed on ice, giving an antibody to virus ratio of 74:1. A similar ratio was used to mix 135S particles and C3 Fabs, also on ice. Some 80S particles were found in the 135S-C3 sample (*22*) and were used to reconstruct the 80S-C3 structure.

Electron Microscopy

Mixtures of poliovirus (160S or 135S) and C3 Fab were suspended over holy carbon films, vitrified, and imaged as described previously (*23*). A CM200 electron microscope (FEI, Hillsboro, Oregon, USA) equipped with Gatan 626 cryoholder (Pleasanton, California, USA) was used. Focal pairs of micrographs were recorded at magnifications of 38,000× at 120 kV.

3-D reconstruction

Particle images were extracted, processed, and normalized as described (*1*). Focal settings

ranged from 0.73 to 1.77 μm underfocus. Focal-pair images were computationally combined for

orientation determination but used separately for origin determination and computation of the 3D

reconstruction. A model determined via common lines (*24*), a previous reconstruction (*1*), and a

135S-C3 map were used to begin iterative model-based determination of orientations and origins

for the 160S-C3, 135S-C3, and 80S-C3 reconstructions, respectively (*25*). Bsoft routines were

used to assess and correct for contrast transfer function (CTF) effects (*26*) via the algorithm by

Conway and Steven (*27*), but images within a focal pair were not combined during CTF

correction. Spherically averaged density plots were used to calibrate size (*26, 28*) against

previously solved structures (*1*) and a poliovirus X-ray crystal structure (*2*).

Modeling

Atomic coordinates for the C3 Fab (*17*) (1FPT in Protein Data Bank) were first fitted manually

("by-eye") into 160S-C3, 135S-C3, and 80S-C3 via UCSF Chimera package (*29*). Next, a core-

weighted, rigid-body fitting algorithm, implemented in CHARRM (*30*), was used to refine the

fits. The full Fab and the antigen-binding or variable domain were refined separately. Each of

the five Fabs was fitted separately to one of the five tips of one mesa. Symmetry was applied via

the UCSF Chimera package (*29*) so that a single Fab binding site contained five overlapping sets

of fitted coordinates for each Fab binding site. Then the overlapping coordinates were averaged

and that average is the fit reported here. The C3 Fab coordinates included a peptide antigen made

of residues 93-103 of poliovirus VP1 (*17*). Residues 97-102 were bound to the Fab in the binding

cleft of the C3 antigen-binding domain, and we compared the positions of these six residues to the corresponding residues in 160S crystal structure (*2*) and the 135S pseudo-atomic model (*4*). Using model and fitted coordinates, we used the match alignment function in UCSF Chimera (*29*) to determine the shift and twist of the BC loop between the 160S and 135S models and the shift and twist between the peptide antigen in the 160S-C3 and 135S-C3 fitted coordinates. This shift and twist was along an axis determined by the algorithm.

4.3 Results

We computed three-dimensional (3D) reconstructions of the 160S-C3, 135S-C3, and 80S-C3 complexes by cryo-EM (Table 4.1). The resolutions of the maps ranged from 9 (for 135S-C3, which was calculated using 9810 particles) to 22 Å (for 80S-C3, which was calculated using 238 particles). 135S and 80S particles were present in the same fields-of-view. These two particle types were picked out separately (from digitized micrographs during particle-image extraction or "boxing", see Methods), and these two data sets were used to compute separate 3D reconstructions.

The 3D reconstructions showed that, as expected, C3 Fab binds to the tip of the mesa– where the BC loop was modeled in the 160S (*2*), 135S (*4*), and 80S (*20*) particle states (Fig. 4.2A-D). Five C3 Fabs surround each mesa, giving it the appearance of a five-petaled flower. C3 Fab density has the same intensity as poliovirus density (Fig. 4.2E), indicating full or nearly full occupancy of all 60 binding sites per virus. The antigen-binding domain in the 135S-C3 density map (Fig. 4.2E) shows the appearance of β-sheets, indicating that the bound Fab is well ordered.

Table 4.1 Microscopy, image reconstruction, and modeling data

Sample	Micrograph pairs[a]	Pixel size (Å)	Particle images[b]	CTF correction[c]	Resolu-tion[d] (Å)	EMDB ID[e]
160S-C3	6	1.82	4184	full	11.1	5291
135S-C3	2	1.84	9810	full	9.1	5292
80S-C3	7	1.84	238	phases only	22	5293

[a]focal pairs, first image taken closer-to-focus, second image farther-from-focus

[b]Total number of images, divide by two for the number of image pairs (focal pairs)

[c]Correction for the final, published reconstruction: full, deconvolution of CTF and correction for decay; or, phases-only, corrected only for the phase-flipping effects of the CTF.

[d]Data set split in two, reconstructions computed and compared via Fourier shell correlation. Resolution determined by the point at which the Fourier shell correlation value reaches 0.5, for reconstructions computed from images were only corrected for phase-flipping of the CTF.

[e]Identification code of density map in EM Data Bank
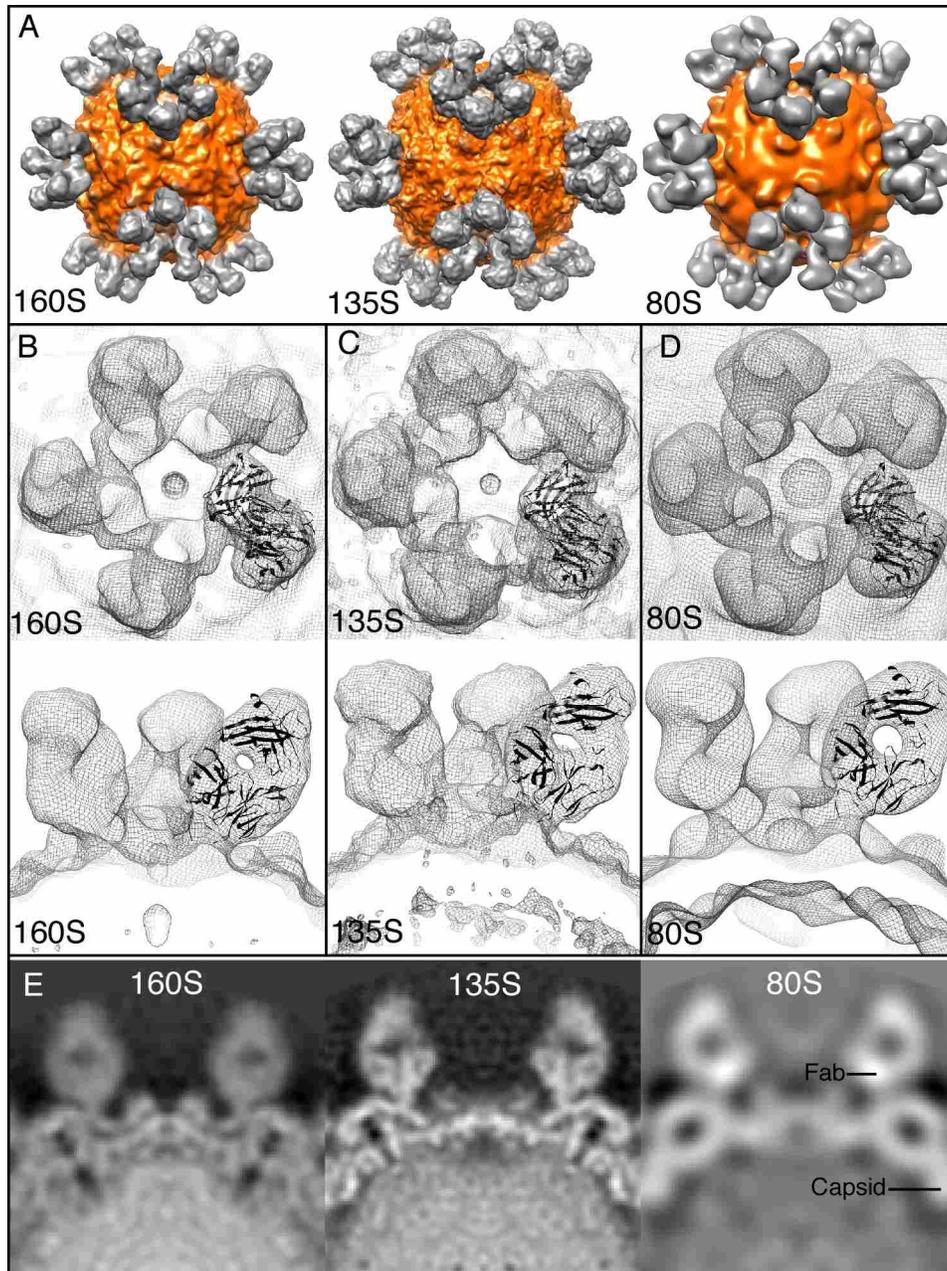
Figure 4.2 Binding of C3 Fab to poliovirus. (A) Cryo-EM structures of 160S-C3 (left), 135S-C3 (middle), and

160SC3 (right). Radial coloring is applied to the surface rendering-density closest to the center of the particle is

orange, density farthest from the center is gray. Here, poliovirus capsids are shown in orange and C3 Fabs are shown

in gray. C3 Fab fitted in 160S-C3 (B), 135S-C3 (C) and 80S-C3 (D) maps. Upper figures show top views, bottom

figures show side views. C3 Fab coordinates (*17*) were fitted into one mesa-bound Fab (black ribbon). Fine mesh is

surface rendering of 3D reconstruction. All maps contoured at 0.5σ. (Contour levels designated by the number of

standard deviations (σ) above the average map density.) (E) Center slices from density maps of C3 complexed with

160S (left) 135S (middle) and 80S (right). 135S-C3 has the highest resolution, followed by 160S-C3 and 80S-C3 (see Table 4.1). Relative density estimates: a sphere of radius = 3 pixels was centered on the designated spots (right panel) and the average density computed. The density of C3 is almost the same as the density of the poliovirus capsid in each case.

C3 Fab coordinates (*17*) were fitted into the cryo-EM density maps and used to deduce changes that occur between 160S, 135S, and 80S particles. The C3 Fab was co-crystallized with a peptide corresponding to part of the BC loop bound in the antigen-binding cleft. Assuming that the Fab binds the free peptide in the same manner as when the BC loop is presented in the context of viral particles, we included the peptide coordinates (corresponding to residues 93 to 103 of VP1) in our fitting to indicate the likely position of the epitope in the poliovirus-C3 complexes. Five regions of C3 Fab density around one fivefold vertex were used to fit coordinates and the average (after symmetry operations to bring four of the five fittings to one position) of all five fits is reported here.

160S-to-135S-to-80S Translational Movements

Comparison of fitted C3 coordinates in the 160S-C3 and 135S-C3 maps indicates that, during the 160S-to-135S transition, the BC-loop antigen changes radius at a similar ratio to undecorated poliovirus (Table 4.2; Figs. 4.2B-D). For example, the distance between the fitted antigenic peptide of C3 Fab and the center of the virus capsid increased 6.7 Å (4.4%) during the transition. Comparing fitted coordinates of the five C3 densities surrounding a single fivefold vertex showed that the distance between the fitted antigenic peptide of C3 Fab and the center of the mesa increased 1.0 Å, 4.0%. These movements are consistent with previous observations of the undecorated 160S and 135S particles, where comparisons of cryo-EM reconstructions showed a 4% expansion along the fivefold axis (*1*). Measurements of published models of the BC loops

71

(*2, 4*) indicated that the distance from the center of the capsid increased 7.0 Å, 4.5%, and the

distance between BC loops and the center of mesa increased 0.9 Å, 4.0%. Therefore,

translational movements of the fitted antigenic peptide in 160S-C3 and 135S-C3 complexes are

consistent with positions of the BC loop in models of 160S (*2*) and 135S (*4*) particles.

Table 4.2 Distance measurements of the fitted antigenic peptide in 160S-C3 and 135S-C3

complexes (bound to antigen-binding domain of C3 Fab[¶]) and BC loop (95-103 residues) in

160S[1] and 135S[2] particle models.

Entity	Model	From "entity" to center of	Average Distance (Å)		Average Increase (%)
			160S-C3 or 160S	135S-C3 or 135S	
Antigenic peptide	Fit into poliovirus-C3Fab	mesa[3]	24.8 ± 0.3	25.8 ± 0.2	4.0
		capsid	152.8 ± 0.3	159.5 ± 0.2	4.4
BC loop	160S[1], 135S[2] coordinates	mesa[3]	22.6	23.5	4.0
		capsid	155.3	162.3	4.5

[¶]Structure from reference (*17*), Protein Data Bank entry 1FPT.

[1]Structure from reference (*2*), Protein Data Bank entry 1ASJ.

[2]Structure from reference (*4*), Protein Data Bank entry 1XYR.

[3]The center of the mesa lies along a fivefold symmetry axis.

In contrast to the large changes in the position of the BC loop in the 160S-to-135S

transition, the fit of the C3 Fab coordinates into the 80S-C3 3D map showed a similar position

and orientation of the Fab to that in the 135S-C3 map (Figs. 4.2C-D), inferring a similar position

of the C3 epitope in the two particle states. The lower resolution of the 80S-C3 map compared

to the 160S-C3 and 135S-C3 maps made the fit of the C3 Fab coordinates less reliable. Hence, a

detailed comparison was impractical. Assuming our fit of the antigen-binding domain of the C3

Fab is a reasonable approximation (Figs. 4.2C-D), the 135S-to-80S transition causes little change

in the position of the C3 antibody.

Antibody binding changes BC loop position

One of the difficulties presented in building models of structures into cryo-EM reconstructions at relatively low resolution is the need to minimize the number of parameters being fit. Except in exceptional cases, this dictates the use of rigid-body approximations for protein subunits, even with structures determined at sub-nanometer resolution. The prominent marker provided by the density for the Fab, and the presence of the peptide corresponding to the BC loop in the C3 Fab crystal structure, provides the opportunity to account for structural changes that take place in the loop and more precisely position it in the models of the 160S-C3 and 135S-C3 complexes.

Using the Fab as a marker, our modeling places the BC loop in a different position with respect to the remainder of VP1 than is observed in the crystal structure of the 160S particle (*2*) or the model of the 135S particle (derived by rigid-body fitting of the capsid proteins to the cryo-EM reconstruction) (*4*) (Fig. 4.3). To measure the deviation, we compared the positions of six residues in the binding cleft of the fitted C3 Fab coordinates with their corresponding position in the 160S (*2*) and 135S (*4*) models. That deviation is approximately 5 Å in both cases (Table 4.3).

Table 4.3 The deviation of residues in the BC loop in 160S[1] and 135S[2] models from the fitted antigenic peptide in 160S-C3 and 135S-C3 complexes.*

Model	Fitting	Absolute distance (in Å) of each Cα atom in 160S[1]/135S[2] residues from the corresponding Cα in respective 160S-C3/135S-C3 fitting							
		97 SER	98 THR	99 THR	100 ASN	101 LYS	102 ASP	Average	Standard Deviation
160S[1]	160S-C3	2.2	2.8	4.0	6.3	8.9	5.7	5.0	2.5
135S[2]	135S-C3	3.6	2.5	4.7	6.5	8.9	5.1	5.2	2.3

[1]Structure from reference (*2*), Protein Data Bank entry 1ASJ.

[2]Structure from reference (*4*), Protein Data Bank entry 1XYR.

*Only the distance between Ca coordinates was measured.
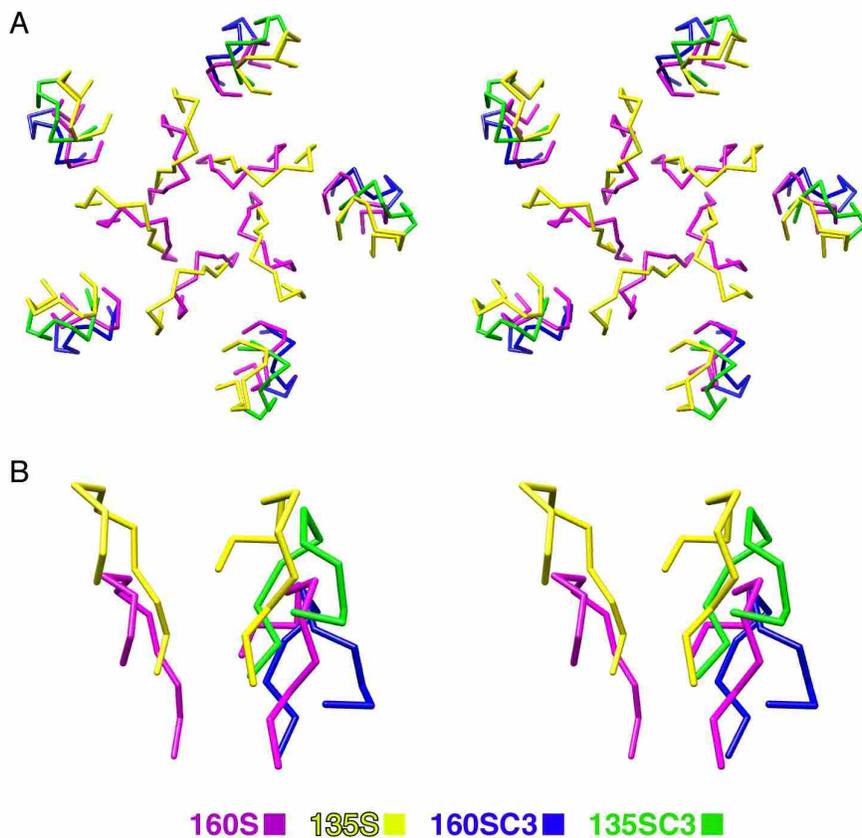
Figure 4.3 Movements of BC loop of poliovirus VP1. Stereo views of BC and DE loops in 160S (magenta) and 135S (yellow), and antigenic peptide found in C3 Fab crystal structure after fitting of Fab coordinates into cryo-EM maps of 160S-C3 (dark blue) and 135S-C3 (green) complexes. DE loops (loop between D and E β-strands of VP1) are shown as a reference. (A) Stereo views of 5 sets of BC (farthest from axis), DE (closest to axis) loops, and fitted antigenic peptides of C3 Fab (far from axis) viewed normal to a 5-fold axis (center of each panel). (B) One set of BC loops, and antigenic peptides of C3 Fab viewed parallel to 5-fold symmetry axis (right side of each panel). DE loops are on the left side of each panel. Although the average deviation of the peptides from the modeled BC loop coordinates is nearly identical (see Table 4.2), the modeled 160S-C3 and 135S-C3 peptides are twisted 15° and shifted 5.6 Å with respect to each other, reflecting the overall twist observed in the antigen-binding domain of the Fab. The change in the BC loops modeled in the X-ray crystal (magenta; Protein Data Bank entry 1ASJ (*2*)) and cryo-EM (yellow; Protein Data Bank entry 1XYR (*4*)) of 160S and 135S particles, respectively, is a twist of 4.6° and shift of 2.6 Å. The corresponding change in the DE loop is a twist of 6° and shift of 4.1 Å. These changes in loop positions were determined via the match function in UCSF Chimera (*29*), which determines rotation and translation parameters to fit one object into another.

Although the C3 Fab crystal coordinates included only a peptide of residues 93-103 (*17*), the BC loop antigen should be bound in a similar position—at least in the antigen-binding cleft. Therefore, the deviation indicates movement of the BC loop upon binding of C3 Fab. Our modeling is based on the fitting of the antigen-binding domain into five symmetry-related positions in the cryo-EM density, and therefore, placement of the antigen-binding cleft (which included the peptide antigen). By placing the symmetry-related subunits in the same asymmetric unit and averaging each fitted set of coordinates to give one average x, y, and z coordinate, we determined an overall average x, y, and z coordinate and determined the fitting error (standard deviation) to be 0.3 and 0.2 Å for the 160S-C3 and 135S-C3 fits, respectively. (We note that the fitting algorithm uses internal density as well as the overall shape of the domain to determine placement of the coordinates (*30*).) We compared bound residues 97-102 in the fitted Fab structures (Cα coordinates only) to their corresponding residues in the BC loop of the 160S crystal structure (*2*) or 135S pseudo-atomic model (*4*). We found a deviation per residue between 2.2 and 8.9 Å (Table 4.3).

The Fab-bound C3 antigen—the BC loop—twists more extensively during the 160S-to-135S transition than was deduced in the 135S pseudo-atomic model (*4*) (Fig. 4.3). Comparison of the 160S-to-135S BC loop change in the X-ray crystal structure of 160S particle and the 135S model showed a rotation of 4.6° and shift of 2.6 Å. Comparison of the same change in the fitted coordinates of the 160S-C3 and 135S-C3 models showed a rotation of 15° and shift of 5.6 Å.

4.4 Discussion

C3 antibody binds to the mesa tip

As expected from previous crystal and cryo-EM studies of 160S, 135S, and 80S particles (*1, 2, 4, 19, 20*), C3 Fab bound to the tip of the 5-fold mesa (Fig. 4.2). The binding affinities of C3 for 160S, 135S and 80S particles are similar (*3*), and we observed similar Fab:capsid density ratios in the 160S-C3, 135S-C3, and 80S-C3 3D maps.

BC loop position is consistent with previous models

As viewed from the antigen-binding domain of the C3 antibody, the 160S-to-135S transition shows an expansion in radius (Table 4.2; Figs. 4.2-3). The expansion of the capsid from 160S to 136S was 4.4 %, as measured by the position of the fitted antigenic peptide in 160S-C3 and 135S-C3 complexes. This measurement is consistent with the expansion of 4.0 % measured previously (*1*). The 80S-C3 structure indicated little, if any, movement of the C3 Fab compared to the C3 position in the 135S-C3 structure, which is also consistent with the previous models of the 135S (*4*) and 80S (*20*) particles.

BC loop is flexible

Residues in the fitted BC-loop peptide deviated 2.2–8.9 Å (average, 5 ± 2 Å) from their positions in the crystal structure of the 160S particle (*2*) and the model of the 135S particle (*4*) (Table 4.3; Fig. 4.3). The low error of the core-weighted fitting (*30*) suggests that the 160S-C3 (error, 0.3 Å) and 135S-C3 (error, 0.2 Å) reconstructions were sufficiently resolved (11 and 9 Å, respectively) to allow such precise fitting and measurement of the BC-loop deviation.

To make the binding interaction stronger and more specific, antibody and antigen may change their conformations during binding (*31*). Binding of antibody to lysozyme induced conformational changes in the antigen and those conformational changes were located at a demonstrably flexible region (*31*). For the interaction of HIV-1 capsid protein p24 with Fab13B5, conformational changes were observed in both antibody and antigen (*32*). For example, Pro207 and Ala208, located in the turn between two helices, moved after Fab binding. Pro207 moved 4 Å, which is comparable to the estimated movement of some residues in the BC loop (Table 4.3). Therefore, because the deviation of the fitted, bound epitope against the BC loop is identical (within experimental error) for the 160S-C3 and 135S-C3 structures (Table 4.3), we postulate that binding of the C3 Fab causes the BC loop to change conformation. The consistent deviation for the 160S-C3 and 135S-C3 structures suggests that the Fab interacts in a similar manner with the two particle states and that the neighboring VP1 structure is also similar for the 160S and 135S particles.

However, our fitting results suggest that the BC loop has a slightly different environment in the 160S and 135S particles. Deviations of the fitted BC loop from the previously modeled loops (*2, 4*) are slightly different in the 160S-C3 and 135S-C3 structures (Table 4.3, Fig. 4.3). For example, during the 160S-to-135S transition, the BC loop in 160S-C3 and 135S-C3 complexes rotates 15° and shifts 5.6 Å, but the BC loop in the X-ray crystal structure of 160S particle and the 135S model only rotates 4.6° and shifts 2.6 Å (Fig. 4.3).

The movement of the BC loop suggests that it is not strongly fixed at a certain conformation, but can easily change its conformation. However, this flexibility is likely not random, but is dictated by interactions with other proteins. In our structures, the conformational change appears to be induced by the antibody-antigen binding interaction (*31*). Such inducible

flexibility may be important in other interactions including cell entry. For example, poliovirus receptor (CD155) is known to also interact with the mesa tip (*33-36*) and a flexible BC loop may be important for that interaction.

Exit of the N-terminus of VP1

During the cell-entry process, receptor binding induces native poliovirus (160S) conversion to the 135S cell-entry intermediate particle (*3, 6*). During this transition, the poliovirus conformation changes with the externalization of membrane-binding entitites VP4 and the N-terminus of VP1. Competing models suggested that the N-terminus of VP1 exited through a channel along the fivefold axis (*37-39*) or at the base of the canyon (*1, 4*). Our results support the latter model.

Although BC loop moves as 160S particle transitions to the 135S particle form, the extent of this movement is inconsistent with the "fivefold exit" model for VP1 and VP4 (*37-39*). The BC loop of VP1 moves less than 1 Å from the center of the mesa (Table 4.2). If the N-terminus of VP1 exits the capsid through the fivefold axis, the BC loop of VP1, and hence the position of C3 Fab, must change significantly. The lack of significant movement supports a model in which the N-terminus of VP1 does not exit through the fivefold axis.

References

1. Belnap, D. M., Filman, D. J., Trus, B. L., Cheng, N., Booy, F. P., Conway, J. F., Curry, S., Hiremath, C. N., Tsang, S. K., Steven, A. C., and Hogle, J. M. (2000) Molecular tectonic model of virus structural transitions: the putative cell entry states of poliovirus, *J. Virol. 74*, 1342-1354.

2. Wien, M. W., Curry, S., Filman, D. J., and Hogle, J. M. (1997) Structural studies of poliovirus mutants that overcome receptor defects, *Nature Struct. Biol. 4*, 666-674.

3. Fricks, C. E., and Hogle, J. M. (1990) Cell-induced conformational change in poliovirus: externalization of the amino terminus of VP1 is responsible for liposome binding, *J. Virol. 64*, 1934-1945.

4. Bubeck, D., Filman, D. J., Cheng, N., Steven, A. C., Hogle, J. M., and Belnap, D. M. (2005) The structure of the poliovirus 135S cell entry intermediate at 10-Angstrom resolution reveals the location of an externalized polypeptide that binds to membranes, *J. Virol. 79*, 7745-7755.

5. Hogle, J. M., and Racaniello, V. R. (2002) *Poliovirus Receptors and Cell Entry*, ASM Press, Washington, D. C.

6. Hogle, J. M. (2002) Poliovirus cell entry: common structural themes in viral cell entry pathways, *Ann. Rev. Microbiol. 56*, 677-702.

7. Levy, H., Bostina, M., Filman, D. J., and Hogle, J. M. (2010) Cell Entry: A Biochemical and Structural Perspective, In *The Picornaviruses* (Ehrenfeld, E., Domingo, E., and Roos, R. P., Eds.), pp 87-104, ASM Press, Washington, DC.

8. Tuthill, T. J., Groppelli, E., Hogle, J. M., and Rowlands, D. J. (2010) Picornaviruses, *Curr Top Microbiol Immunol 343*, 43-89.

9. Blondel, B., Akacem, O., Crainic, R., Couillin, P., and Horodniceanu, F. (1983) Detection by monoclonal antibodies of an antigenic determinant critical for poliovirus neutralization present on VP1 and on heat-inactivated virions, *Virology 126*, 707-710.

10. Wychowski, C., van der Werf, S., Siffert, O., Crainic, R., Bruneau, P., and Girard, M. (1983) A poliovirus type 1 neutralization epitope is located within amino acid residues 93 to 104 of viral capsid polypeptide VP1, *EMBO J 2*, 2019-2024.

11. van der Werf, S., Wychowski, C., Bruneau, P., Blondel, B., Crainic, R., Horodniceanu, F., and Girard, M. (1983) Localization of a poliovirus type 1 neutralization epitope in viral capsid polypeptide VP1, *Proc. Natl. Acad. Sci. USA 80*, 5080-5084.

12. Minor, P. D., Schild, G. C., Bootman, J., Evans, D. M. A., Ferguson, M., Reeve, P., Spitz, M., Stanway, G., Cann, A. J., Hauptmann, R., Clarke, L. D., Mountford, R. C., and Almond, J. W. (1983) Location and primary structure of a major antigenic site for poliovirus neutralization, *Nature 301*, 674-679.

13. Emini, E. A., Jameson, B. A., and Wimmer, E. (1983) Priming for and induction of anti-poliovirus neutralizing antibodies by synthetic peptides, *Nature 304*, 699-703.

14. Evans, D. M. A., Minor, P. D., Schild, G. S., and Almond, J. W. (1983) Critical role of an eight-amino acid sequence of VP1 in neutralization of poliovirus type 3, *Nature 304*, 459-462.

15. Chow, M., Yabrov, R., Bittle, J., Hogle, J., and Baltimore, D. (1985) Synthetic peptides from four separate regions of the poliovirus type 1 capsid protein VP1 induce neutralizing antibodies, *Proc Natl Acad Sci U S A 82*, 910-914.

16. Horaud, F., Crainic, R., Vanderwerf, S., Blondel, B., Wichowski, C., Akacem, O., Bruneau, P., Couillin, P., Siffert, O., and Girard, M. (1987) Identification and characterization of a continuous neutralization epitope (C3) present on type 1 poliovirus, *Prog Med Virol 34*, 129-155.

17. Wien, M. W., Filman, D. J., Stura, E. A., Guillot, S., Delpeyroux, F., Crainic, R., and Hogle, J. M. (1995) Structure of the complex between the Fab fragment of a neutralizing antibody for type 1 poliovirus and its viral epitope, *Nature Struct. Biol. 2*, 232-243.

18. Filman, D. J., Syed, R., Chow, M., Macadam, A. J., Minor, P. D., and Hogle, J. M. (1989) Structural factors that control conformational transitions and serotype specificity in type 3 poliovirus, *EMBO J 8*, 1567-1579.

19. Hogle, J. M., Chow, M., and Filman, D. J. (1985) Three-dimensional structure of poliovirus at 2.9 Å resolution, *Science 229*, 1358-1365.

20. Levy, H. C., Bostina, M., Filman, D. J., and Hogle, J. M. (2010) Catching a virus in the act of RNA release: a novel poliovirus uncoating intermediate characterized by cryo-electron microscopy, *J Virol 84*, 4426-4441.

21. Rueckert, R. R., and Pallansch, M. A. (1981) Preparation and characterization of encephalomyocarditis (EMC) virus, In *Interferons* (Pestka, S., Ed.), pp 315-325, Academic Press, New York.

22. Curry, S., Chow, M., and Hogle, J. M. (1996) The poliovirus 135S particle is infectious, *J. Virol. 70*, 7125-7131.

23. Zlotnick, A., Cheng, N., Conway, J. F., Booy, F. P., Steven, A. C., Stahl, S. J., and Wingfield, P. T. (1996) Dimorphism of Hepatitis B Virus Capsids Is Strongly Influenced by the C-Terminus of the Capsid Protein, *Biochemistry 35*, 7412-7421.

24. Fuller, S. D., Butcher, S. J., Cheng, R. H., and Baker, T. S. (1996) Three-dimensional reconstruction of icosahedral particles--the uncommon line, *J. Struct. Biol. 116*, 48-55.

25. Baker, T. S., and Cheng, R. H. (1996) A model-based approach for determining orientations of biological macromolecules imaged by cryo-electron microscopy, *J. Struct. Biol. 116*, 120-130.

26. Heymann, J. B., and Belnap, D. M. (2007) Bsoft: image processing and molecular modeling for electron microscopy, *J. Struct. Biol. 157*, 3-18.

27. Conway, J. F., and Steven, A. C. (1999) Methods for reconstructing density maps of 'single' particles from cryoelectron micrographs to subnanometer resolution, *J. Struct. Biol. 128*, 106-118.

28. Belnap, D. M., Grochulski, W. D., Olson, N. H., and Baker, T. S. (1993) Use of radial density plots to calibrate image magnification for frozen-hydrated specimens, *Ultramicroscopy 48*, 347-358.

29. Pettersen, E. F., Goddard, T. D., Huang, C. C., Couch, G. S., Greenblatt, D. M., Meng, E. C., and Ferrin, T. E. (2004) UCSF chimera - A visualization system for exploratory research and analysis, *Journal of Computational Chemistry 25*, 1605-1612.

30. Wu, X., Milne, J. L., Borgnia, M. J., Rostapshov, A. V., Subramaniam, S., and Brooks, B. R. (2003) A core-weighted fitting method for docking atomic structures into low-resolution maps: application to cryo-electron microscopy, *J Struct Biol 141*, 63-76.

31. Davies, D. R., and Cohen, G. H. (1996) Interactions of protein antigens with antibodies, *Proc Natl Acad Sci U S A 93*, 7-12.

32. Monaco-Malbet, S., Berthet-Colominas, C., Novelli, A., Battai, N., Piga, N., Cheynet, V., Mallet, F., and Cusack, S. (2000) Mutual conformational adaptations in antigen and antibody upon complex formation between an Fab and HIV-1 capsid protein p24, *Structure 8*, 1069-1077.

33. Belnap, D. M., McDermott, B. M., Jr., Filman, D. J., Cheng, N., Trus, B. L., Zuccola, H. J., Racaniello, V. R., Hogle, J. M., and Steven, A. C. (2000) Three-dimensional structure of poliovirus receptor bound to poliovirus, *Proc. Natl. Acad. Sci. USA 97*, 73-78.

34. He, Y. N., Bowman, V. D., Mueller, S., Bator, C. M., Bella, J., Peng, X. H., Baker, T. S., Wimmer, E., Kuhn, R. J., and Rossmann, M. G. (2000) Interaction of the poliovirus receptor with poliovirus, *Proc Natl Acad Sci U S A 97*, 79-84.

35. Xing, L., Tjarnlund, K., Lindqvist, B., Kaplan, G. G., Feigelstock, D., Cheng, R. H., and Casasnovas, J. M. (2000) Distinct cellular receptor interactions in poliovirus and rhinoviruses, *EMBO Journal 19*, 1207-1216.

36. Zhang, P., Mueller, S., Morais, M. C., Bator, C. M., Bowman, V. D., Hafenstein, S., Wimmer, E., and Rossmann, M. G. (2008) Crystal structure of CD155 and electron microscopic studies of its complexes with polioviruses, *Proc. Natl. Acad. Sci. USA 105*, 18284-18289.

37. Giranda, V. L., Heinz, B. A., Oliveira, M. A., Minor, I., Kim, K. H., Kolatkar, P. R., Rossmann, M. G., and Rueckert, R. R. (1992) Acid-induced structural changes in human rhinovirus 14: possible role in uncoating, *Proc Natl Acad Sci U S A 89*, 10213-10217.

38. Hewat, E. A., and Blaas, D. (2004) Cryoelectron microscopy analysis of the structural changes associated with human rhinovirus type 14 uncoating, *J. Virol. 78*, 2935-2942.

39. Kolatkar, P. R., Bella, J., Olson, N. H., Bator, C. M., Baker, T. S., and Rossmann, M. G. (1999) Structural studies of two rhinovirus serotypes complexed with fragments of their cellular receptor, *EMBO J 18*, 6249-6259.

Chapter 5. Structure of the Fab-Labeled "Breathing" State of Native Poliovirus

5.1 Introduction

A protein "breathes" when it changes its conformation in reversible patterns. Such reversible conformational changes may be necessary for some proteins to function properly.

The viral capsids of some non-enveloped viruses are dynamic structures with reversible exposure of internal, unexposed amino-acid sequences under physiological conditions. This dynamic behavior is often termed "breathing". "Breathing" non-enveloped viruses include picornaviruses, such as poliovirus (*1, 2*), human rhinovirus 14 (HRV14) (*3, 4*), HRV16 (*4*), swine vesicular disease virus (*5*), and coxsackievirus (*6*); nodaviruses, such as Flock House virus (FHV) (*7*); tetraviruses, such as *Nudaurelia ω capensis* and *Helicoverpa armigera* stunt virus (*8*); bromoviruses, such as cowpea chlorotic mottle virus (*9*); tombusviruses, such as tomato bushy stunt virus (*10, 11*); and sobemoviruses, such as southern bean mosaic virus (*12*). Transient, reversible exposition of internal proteins may be an important step for the cell-entry process, especially for conformational changes required to insert internal, hydrophobic, membrane-binding peptides into the membrane (*13-15*).

"Breathing" in poliovirus was first discovered when antibodies to normally internal amino-acid sequences, VP4 and the N-terminus of VP1, were found to bind to native particles (*1, 2*). The studies suggested that capsid "breathing" represented large dynamic changes in virion structure at 37 ºC. To study this purported structure and mark the exposed N-terminus of VP1, we utilized cryogenic electron microscopy (cryo-EM) and three-dimensional image reconstruction to observe the structure of viruses incubated at 37 ºC with an Fab of a monoclonal antibody to the designated region (*2, 16*).

5.2 Materials and Methods

Poliovirus 1/Mahoney was grown and purified as described previously (*17, 18*). From a preparation of monoclonal antibodies targeted to amino acids 39 to 55 of poliovirus type 1/Mahoney VP1 (*2*), Fab was prepared by the ImmunoPure® Fab preparation kit (Pierce, Thermo Fisher Scientific, Rockford, Illinois, USA). Solutions of native poliovirus (sedimentation coefficient 160S) and Fab were mixed at 37 ºC with an antibody-to-virus ratio of 95:1 and incubated at 37 ºC for 2 hours.

Poliovirus-Fab mixture was suspended over holy carbon films. The grid was plunge-frozen using an FEI Vitrobot (Hillsboro, Oregon, USA). The mixture was kept at 37 ºC until the sample was plunge frozen. In the microscope, the grid was kept cold by a Gatan 626 cryoholder (Pleasanton, California, USA), and micrographs were recorded on an FEI Tecnai F30 transmission electron microscope (Hillsboro, Oregon, USA) at magnification of 39,000× at 300 kV. The films were scanned with a Nikon 9000 ED film scanner (Tokyo, Japan).

Particle images were extracted with the X3DPREPROCESS program (*19*). The Bsoft package was applied to determine and correct for contrast transfer function (CTF) effects (*20*) via the algorithm by Conway and Steven (*21*). Focal settings ranged from 2.40 to 3.03 μm underfocus. The PFT2 iterative model-based determination of orientations and origins (*22, 23*) was used, and previous reconstructions of native poliovirus (sedimentation coefficient,160S) (D.M. Belnap et al., unpublished) and the cell-entry intermediate (135S) particle (*24*) were the starting models. A Fourier-Bessel algorithm was used to compute the 3D reconstruction (*25*). Despite differences in the starting models, the capsid structure, the Fab density location and volume, and the center slice of the two resulting maps were nearly identical. Because the capsid structure and the RNA shape shown in the center slice of the map appeared more like the 135S

particle than 160S particle, the map reconstructed by using the 135S particle as the starting

model was used for further image processing steps. In the micrograph, some 160S particles

appeared to have few or no Fab bound (data not shown). A previously determined, undecorated

poliovirus cryo-EM density map (particles at room temperature or lower before plunge freezing)

(D.M. Belnap et al., unpublished) and the initial 160S-37 °-Fab reconstruction served as the

starting models for multiple-model-based classification (*26*). Each particle image was compared

to a model projection from each state. Selected particles had a minimum difference of 0.04 in

the correlation-coefficient value between the correlation coefficients obtained from each form.

Finally, 137 particles were selected to reconstruct the structure of the 160S 37 °C "breathing"

state with Fab bound to a resolution of 25 Å.

5.3 Results and Discussion

Aggregation of particles was observed in cryo-EM micrograph. A cryo-EM micrograph of

160S (Fig. 5.1B) showed a relatively smooth outer capsid surface. On the other hand, the cryo-

EM micrograph of 160S complexed with Fab incubated at 37 °C for 2 hours (Fig. 5.1A) showed

that the capsid surface was not smooth and contained additional density, which indicates bound

Fab, externalized VP4 or the N-terminus of VP1, or both bound Fab and externalized

polypeptide. These particles were inclined to aggregate (Fig. 5.1A). Hydrophobic portions of

externalized peptides may cause the observed aggregation (*14*).

Exposed peptides in "breathing" structure are near the twofold axis. At low contour level,

the density map of the 160S-Fab complex at 37 ºC (Fig. 5.2A) showed that the Fab-binding site

is close to the 2-fold axis, which indicates that the N-terminus of VP1 exits from the internal

capsid at the 2-fold axis in the poliovirus "breathing" state. The Fab density on the capsid is very weak (Figs. 5.2A,E), which is due to the low occupancy of Fab on the capsid; the lack of a defined Fab also indicates that the epitope is flexible (Lin et al., unpublished). The percentage of the 60 subunits bound with Fab cannot be determined. The antibody used in this study showed a stronger binding affinity with 135S and genome-released (80S) particles than with 160S particles (*2*), which may occur because of the reversible transient externalization of N-terminus of VP1 or the partial exposure of the peptide epitopes in the 160S "breathing" state. We note that exposed polypeptides may contribute to the extra density we observed in the 160S-37 °-Fab complex (Figs. 5.2A,E). Fab density likely makes up the largest portion despite the lack of complete correspondence with the shape of an Fab.

At 37 °C, 160S likely has a dynamic structure because of the reversible externalization of the internal peptides. Therefore, externalized polypeptides in the "breathing" state probably have multiple conformations. The 160S-37°-Fab complex reported here may be an average of multiple "breathing" states or only one of multiple "breathing" states. The relatively low resolution of the map suggests that multiple conformations were averaged.
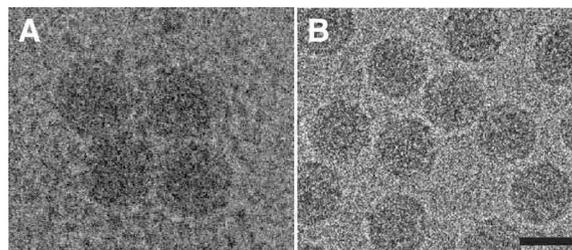

Figure 5.1 Electron micrographs of frozen-hydrated poliovirus. (A) A complex of 160S and Fab to the 39-55 residues of VP1 incubated at 37 ºC for 2 hours. (B) 160S particles. Bar = 30 nm.
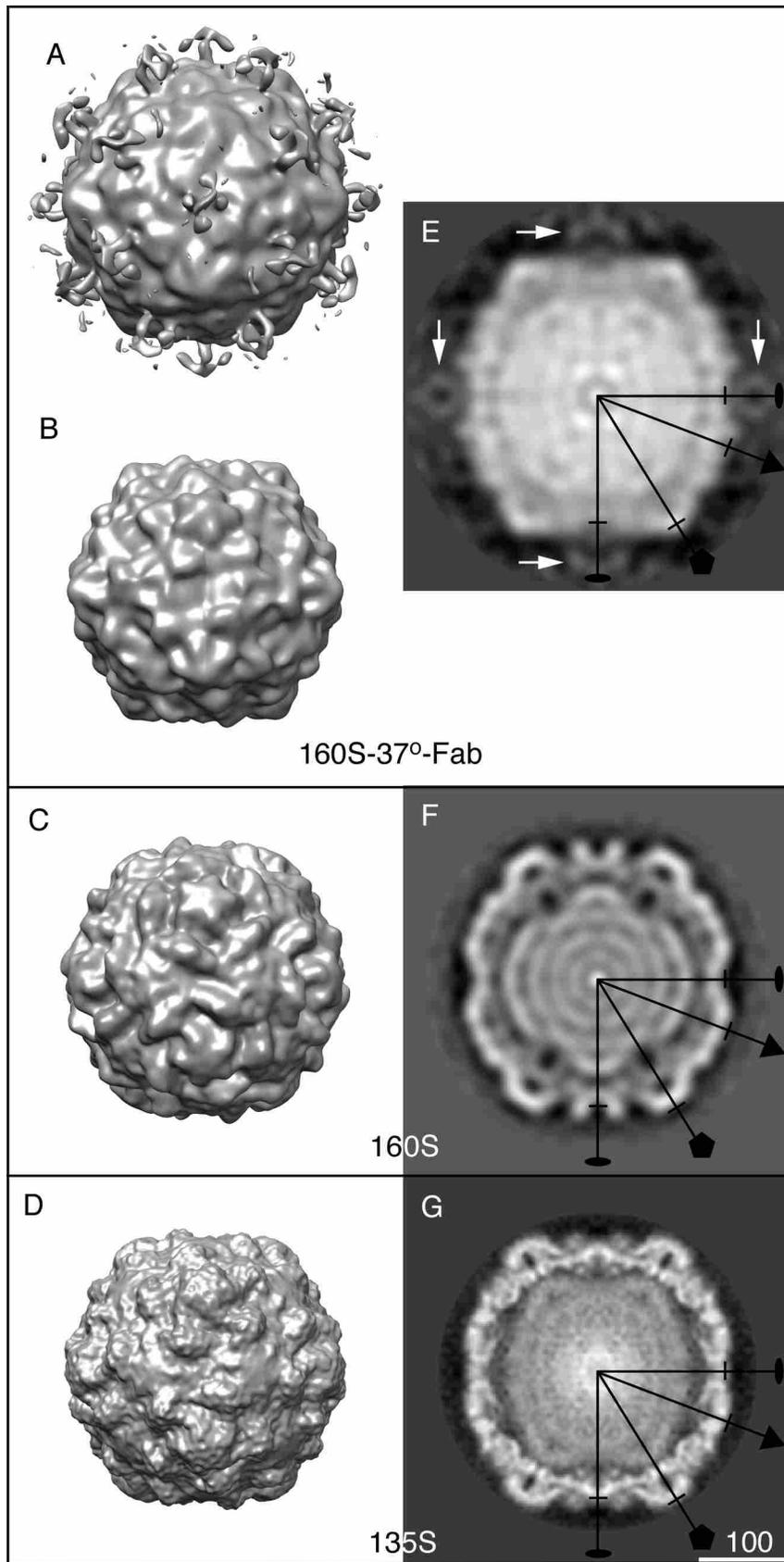
160S-37°-Fab

160S

135S

100

Figure 5.2 Structure of 160S-37º-Fab complex compared to 160S and 135S particles. Surface representations of the three-dimensional structures of 160S-Fab complex at 37 ºC (A-B). 160S and Fab to the 39-55 residues of VP1 were incubated at 37 °C for 2 hours. 160S-37º-Fab complex reconstructions at resolution 25 Å at contour levels of 0σ (A) and 1.3σ (B). 160S (D.M. Belnap et al., unpublished) (C) and 135S (*27*) (D) maps are shown at contour level 0σ. Central sections of the poliovirus 160S-37º-Fab complex (E), 160S (F), and 135S (G) reconstructions. The sections are perpendicular to the twofold symmetry axes. Fab densities are on the twofold axes (white arrows). Some symmetry axes are labeled. The markers perpendicular to each symmetry axis, 5-fold (pentagon), 3-fold (triangle), and 2-fold (oval), show the radius of the 160S structure. Scale bar for panels E, F and G = 100 Å.

Comparison of reversible "breathing" and irreversible 160S-to-135S changes. During cell entry, poliovirus receptor (CD155) interacts with a 160S particle and induces the formation of the intermediate 135S particle (*18, 28*). This transition includes the irreversible externalization of VP4 and the N-terminus of VP1 from the internal side of the capsid (*18, 28*). Previous authors have asked whether the reversible exposition of these same polypeptides during "breathing" is similar to the irreversible changes that occur in the 160S-to-135S transition (*1, 15*).

The structure of the 160S-37°-Fab complex (Fig. 5.2B) differs from the 160S structure (Fig. 5.2C). By comparing central density slices of 160S-37°-Fab, 160S, and 135S maps (Fig. 5.2E-G), we observed that the 160S-37°-Fab capsid is ~7% larger than 160S and ~4% larger than 135S at the fivefold axis, ~1% larger than 160S and ~3% smaller than 135S at the twofold axis, but nearly same as 160S and 135S at the threefold axis. These comparisons are similar to the difference between the 135S and 160S particle states observed previously (*24*). The shape of the RNA in the 160S-37°-Fab complex appears more similar to that in the 135S particle than the RNA in the 160S structure (Fig. 5.2E-G). Therefore, the 160S "breathing" structure resembles the 135S state in at least two significant features.

VP4 and the N-terminus of VP1 were observed to externalize from the internal poliovirus capsid in the 160S "breathing" process and in 160S-to-135S transition (*29, 30*). The expansion of the capsid may facilitate externalization of the internal peptides (*15*). Functionally, the externalization of internal amino-acid sequences in 160S-to-135S transition is similar to externalization of the same sequences in the "breathing" process of poliovirus (*1, 15*), which may be the reason that the 160S-37º-Fab map is similar to the 135S map (Fig. 5.2). Bound Fab may stabilize externalization of the internal peptides (VP4 and the N-terminus of VP1) and keep these particles in the "breathing" state.

However, the conformational change from the 160S "closed" state to 160S "breathing" state or to 135S differs. At 37 °C, the internal protein exits the capsid reversibly in 160S "breathing" state. In the 160S-to-135S transition, the irreversible conformational change leads the permanent externalization. The 160S X-ray crystal structure (*31*) showed that residues 39-55 spans the inside of the capsid from the propeller edge to near the 2-fold axis depression. The 160S-37 º-Fab map (Fig. 5.2A) showed the N-terminus of VP1 exits from the internal capsid at the 2-fold axis in the poliovirus "breathing" state. In the 135S cryo-EM model (*27*), only residues 42-52 were shown, which were located at the canyon between the mesa and propeller tip. The V8-cleaved 135S (*27*) or 135S-Fab complex (Fab binds to the 24-40 residues of VP1) (Lin et al., submitted) showed that the N-terminus of VP1 locates at the propeller tip. The different location of the N-terminus of VP1 in the 160S "breathing" state and 135S particle indicates that these two externalization of internal sequence processes are distinct. Some antiviral drugs can inhibit the formation of 135S particles but cannot inhibit the formation of the "breathing" state of 160S particles, which indicated that the poliovirus "breathing" differs from the formation of 135S (*1*). Nevertheless, as previously noted (*15*), "breathing" indicates a dynamic capsid

structure that is primed to undergo irreversible changes. Perhaps activation by the poliovirus-receptor interaction or heating (*18, 32*) is, in forming the 135S particle, able to direct the N-terminus in a different direction from the reversible exposure observed at 37 °C.

The 160S-37º-Fab complex and 135S particle (*27, 30*) show that externalization of the internal sequences is linked to or concurrent with capsid expansion. The different location of N-terminus of VP1 on 160S capsid in "breathing" state and 135S capsid indicates that externalization has two pathways and may have different roles in "breathing" and cell entry.

References

1. Li, Q., Yafal, A. G., Lee, Y. M., Hogle, J., and Chow, M. (1994) Poliovirus neutralization by antibodies to internal epitopes of VP4 and VP1 results from reversible exposure of these sequences at physiological temperature, *J Virol 68*, 3965-3970.

2. Roivainen, M., Piirainen, L., Rysa, T., Narvanen, A., and Hovi, T. (1993) An immunodominant N-terminal region of VP1 protein of poliovirion that is buried in crystal structure can be exposed in solution, *Virology 195*, 762-765.

3. Lewis, J. K., Bothner, B., Smith, T. J., and Siuzdak, G. (1998) Antiviral agent blocks breathing of the common cold virus, *Proc Natl Acad Sci U S A 95*, 6774-6778.

4. Katpally, U., Fu, T. M., Freed, D. C., Casimiro, D. R., and Smith, T. J. (2009) Antibodies to the buried N terminus of rhinovirus VP4 exhibit cross-serotypic neutralization, *J Virol 83*, 7040-7048.

5. Jimenez-Clavero, M. A., Douglas, A., Lavery, T., Garcia-Ranea, J. A., and Ley, V. (2000) Immune recognition of swine vesicular disease virus structural proteins: novel antigenic regions that are not exposed in the capsid, *Virology 270*, 76-83.

6. Pulli, T., Lankinen, H., Roivainen, M., and Hyypia, T. (1998) Antigenic sites of coxsackievirus A9, *Virology 240*, 202-212.

7. Bothner, B., Dong, X. F., Bibbs, L., Johnson, J. E., and Siuzdak, G. (1998) Evidence of viral capsid dynamics using limited proteolysis and mass spectrometry, *J Biol Chem 273*, 673-676.

8. Bothner, B., Taylor, D., Jun, B., Lee, K. K., Siuzdak, G., Schultz, C. P., and Johnson, J. E. (2005) Maturation of a tetravirus capsid alters the dynamic properties and creates a metastable complex, *Virology 334*, 17-27.

9. Speir, J. A., Bothner, B., Qu, C., Willits, D. A., Young, M. J., and Johnson, J. E. (2006) Enhanced local symmetry interactions globally stabilize a mutant virus capsid that maintains infectivity and capsid dynamics, *J Virol 80*, 3582-3591.

10. Jaegle, M., Briand, J. P., Burckard, J., and Van Regenmortel, M. H. (1988) Accessibility of three continuous epitopes in tomato bushy stunt virus, *Ann Inst Pasteur Virol 139*, 39-50.

11. Witz, J., and Brown, F. (2001) Structural dynamics, an intrinsic property of viral capsids, *Arch Virol 146*, 2263-2274.

12. Mackenzie, D. J., and Tremaine, J. H. (1986) The Use of a Monoclonal-Antibody Specific for the N-Terminal Region of Southern Bean Mosaic-Virus as a Probe of Virus Structure, *J Gen Virol 67*, 727-735.

13. Hendry, E., Hatanaka, H., Fry, E., Smyth, M., Tate, J., Stanway, G., Santti, J., Maaronen, M., Hyypia, T., and Stuart, D. (1999) The crystal structure of coxsackievirus A9: new insights into the uncoating mechanisms of enteroviruses, *Structure 7*, 1527-1538.

14. Johnson, J. E. (2003) Virus particle dynamics, *Adv Protein Chem 64*, 197-218.

15. Hogle, J. M. (2002) Poliovirus cell entry: common structural themes in viral cell entry pathways, *Annu Rev Microbiol 56*, 677-702.

16. Hovi, T., and Roivainen, M. (1993) Peptide antisera targeted to a conserved sequence in poliovirus capsid VP1 cross-react widely with members of the genus Enterovirus, *J Clin Microbiol 31*, 1083-1087.

17. Rueckert, R. R., and Pallansch, M. A. (1981) Preparation and characterization of encephalomyocarditis (EMC) virus, In *Interferons* (Pestka, S., Ed.), pp 315-325, Academic Press, New York.

18. Curry, S., Chow, M., and Hogle, J. M. (1996) The poliovirus 135S particle is infectious, *J. Virol. 70*, 7125-7131.

19. Conway, J. F., Trus, B. L., Booy, F. P., Newcomb, W. W., Brown, J. C., and Steven, A. C. (1993) The effects of radiation damage on the structure of frozen hydrated HSV-1 capsids, *J Struct Biol 111*, 222-233.

20. Heymann, J. B., and Belnap, D. M. (2007) Bsoft: image processing and molecular modeling for electron microscopy, *J. Struct. Biol. 157*, 3-18.

21. Conway, J. F., and Steven, A. C. (1999) Methods for reconstructing density maps of 'single' particles from cryoelectron micrographs to subnanometer resolution, *J. Struct. Biol. 128*, 106-118.

22. Baker, T. S., and Cheng, R. H. (1996) A model-based approach for determining orientations of biological macromolecules imaged by cryo-electron microscopy, *J. Struct. Biol. 116*, 120-130.

23. Sanz-García, E., Stewart, A. B., and Belnap, D. M. (2010) The random-model method enables *ab initio* three-dimensional reconstruction of asymmetric particles and determination of particle symmetry, *J. Struct. Biol. 171*, 216-222.

24. Belnap, D. M., Filman, D. J., Trus, B. L., Cheng, N., Booy, F. P., Conway, J. F., Curry, S., Hiremath, C. N., Tsang, S. K., Steven, A. C., and Hogle, J. M. (2000) Molecular tectonic model of virus structural transitions: the putative cell entry states of poliovirus, *J. Virol. 74*, 1342-1354.

25. Fuller, S. D., Butcher, S. J., Cheng, R. H., and Baker, T. S. (1996) Three-dimensional reconstruction of icosahedral particles--the uncommon line, *J. Struct. Biol. 116*, 48-55.

26. Heymann, J. B., Conway, J. F., and Steven, A. C. (2004) Molecular dynamics of protein complexes from four-dimensional cryo-electron microscopy, *J. Struct. Biol. 147*, 291-301.

27. Bubeck, D., Filman, D. J., Cheng, N., Steven, A. C., Hogle, J. M., and Belnap, D. M. (2005) The structure of the poliovirus 135S cell entry intermediate at 10-Angstrom resolution reveals the location of an externalized polypeptide that binds to membranes, *J. Virol. 79*, 7745-7755.

28. Huang, Y., Hogle, J. M., and Chow, M. (2000) Is the 135S poliovirus particle an intermediate during cell entry?, *J Virol 74*, 8757-8761.

29. Chow, M., Newman, J. F., Filman, D., Hogle, J. M., Rowlands, D. J., and Brown, F. (1987) Myristylation of picornavirus capsid protein VP4 and its structural significance, *Nature 327*, 482-486.

30. Fricks, C. E., and Hogle, J. M. (1990) Cell-induced conformational change in poliovirus: externalization of the amino terminus of VP1 is responsible for liposome binding, *J. Virol. 64*, 1934-1945.

31. Wien, M. W., Curry, S., Filman, D. J., and Hogle, J. M. (1997) Structural studies of poliovirus mutants that overcome receptor defects, *Nat Struct Biol 4*, 666-674.

32. Kaplan, G., Freistadt, M. S., and Racaniello, V. R. (1990) Neutralization of poliovirus by cell

receptors expressed in insect cells, *J Virol 64*, 4697-4702.

Chapter 6. Conclusion and Future Work

6.1 Conclusion

In Chapter 1 and 2, I explained the biological properties of poliovirus, the current understanding of poliovirus cell entry, the methodology of cryo-EM biomolecular structure analysis and the use of antibodies to detect antigen location. This is the basis of my research. My research target is poliovirus, the main technique I used to obtain the 3D structure of poliovirus-Fab complexes is cryogenic electron microscopy (cryo-EM) and three-dimensional image reconstruction, specifically single-particle analysis. I used three different antibodies to track different portions of the N-terminus of VP1 in poliovirus particles to understand more about poliovirus cell entry.

In Chapter 3, The Fab fragment of a monospecific "P1" antibody, which was raised against a peptide corresponding to N-terminal residues 24-40 of VP1, was utilized to track the location of the N-terminus of VP1 in the 135S and 80S states of poliovirus particles. On 135S, P1 Fabs bind to a prominent feature on the external surface known as the "propeller tip". In contrast, our initial 80S-P1 reconstruction showed P1 Fabs also binding to a second site, ~60 Å distant, at the icosahedral twofold axes. Further analysis showed that the overall population of 80S-P1 particles consisted of three kinds of capsids: those with P1 Fabs bound only at the propeller tips; only at the twofold axes; or simultaneously at both positions. Our results indicate that, in 80S particles, a significant fraction of VP1 can deviate from icosahedral symmetry. Hence, this portion of VP1 does not change conformation synchronously when switching from the 135S state. These conclusions are compatible with previous observations of multiple conformations of the 80S state and suggest that movement of the N-terminus of VP1 has a role in

uncoating. Similar deviations from icosahedral symmetry may be biologically significant during other viral transitions.

In Chapter 4, we tracked the location of the external BC loop of VP1 (residues 95-105) in 160S, 135S, and 80S particles by labeling them with the C3 monoclonal antibody, determining their three-dimensional structures by cryogenic electron microscopy (cryo-EM), and fitting atomic-resolution coordinates into the resulting density maps. The C3 epitope, located on the tip of a prominent peak known as the "mesa", shifts outwards in radius by 4.5% and twists through 15° in the 160S-to-135S transition, but appears unchanged in the 135S-to-80S transition. In addition, binding of C3 to either 160S or 135S particles causes residues of the BC loop to move an estimated 5 (±2) Å, indicating flexibility. The flexibility of this loop may play a role in cell-entry interactions and give us structural information for antiviral drug design. A potential antiviral drug, which can bind and stabilize the BC loop, may prevent receptor binding and inhibit cell entry.

In Chapter 5, An Fab fragment of a monoclonal antibody, binding to the residues 39-55 of VP1, was utilized to track the location of the N-terminus of VP1 in the native (160S) particle in this "breathing" state. At 37 °C, the structure of poliovirus is dynamic, and internal polypeptides VP4 and the N-terminus of VP1 externalize reversibly, which is "capsid breathing". Fab and virus were mixed at 37 ºC and imaged via cryogenic electron microscopy. The resulting reconstruction showed the capsid expands similarly to the irreversibly altered cell-entry intermediate (135S) particle, but the N-terminus of VP1 is located near the twofold axes, instead of the propeller tip as in 135S particles.

6.2 Future Work

6.2.1 Further studies on poliovirus

160S "breathing" structure at high resolution

The 160S "breathing" structure shown in Chapter 5 is at 25-Å resolution. A higher resolution

(represented by a lower numerical value) structure would give more information. To obtain a

high-resolution "breathing" structure, Fabs which bind to the N-terminus of poliovirus VP1 with

a higher affinity than those used in Chapter 5 could prove beneficial. At 37 ºC, the 160S particles

will have a higher occupancy of Fab, due to its greater affinity, this might allow a greater

population of 160S particles to stay at a certain "breathing" state. These more tightly bound

160S-Fab particles will produce a higher resolution 3D reconstruction because more of them will

be in a uniform state.

More comparison data between 160S particles in "breathing" state and 135S particles

The position of residues 39-55 of the N-terminus of VP1 in 160S "breathing" particles is shown

by the 160S-37º-Fab map (see Chapter 5) while the position of the N-terminus of VP1 in 135S is

shown by V8-cleaved 135S maps (showing the location of the first 31 residues of VP1 (*1*)) and

135S-P1 maps (showing the location of residues 24-40 of VP1, see Chapter 3). A 135S-Fab (Fab

binding to residues 39-55 of the N-terminus of poliovirus VP1) structure would allow us to

directly compare the antigen position in 160S "breathing" particles and 135S particles. I did

some preliminary work for the reconstruction of this 135S-Fab complex, but more work needs to

be done.

Identification of the exposed peptides in 160S "breathing" particles and 135S particles by mass spectrometry

The high sensitivity and accuracy of matrix-assisted laser desorption/ionization mass spectrometry (MALDI-MS) make it a useful method for identifying the proteolysis products of viruses. For example, the results of limited proteolysis/MALDI-MS on HRV14 and FHV showed that internal peptides are part of the solvent-accessible domain and are transiently present on the capsid surface (*2, 3*). Limited proteolysis/MALDI-MS is another method that can be used on 160S "breathing" particles and 135S particles to identify the exposed residues from the N-terminus of VP1. If the MALDI-MS experiment was run on both types of particles, the exposed residues could be compared. This would further clarify the biological similarity or difference between the reversible externalization of VP1 in 160S "capsid breathing" and the irreversible externalization of VP1 during the 160S-to-135S transition.

6.2.2 Application of the Fab-labeling technique to other systems

Poliovirus is the only nonenveloped virus in which I studied the externalization of the internal capsid proteins of the noneveloped virus. Cell entry of nonenveloped viruses is not well understood, but often involves externalization of internally located peptides. For example, this occurs in human rhinovirus 2 (HRV2) (*4*), HRV16 (*5*) and FHV (*3*). Future work could apply similar methods (to track the externalization via virus-antibody interactions with cryo-EM) as I showed in Chapters 2-5 on the HRV2, HRV16 and FHV systems to observe where the internal capsid proteins exit from the capsid.

HRVs belong to the picornavirus family and are the most frequent cause of the common cold. HRVs are classified into two groups depending on their cellular receptors. The intercellular

adhesion molecule 1 (ICAM-1 or CD54) is the receptor for the major group, and members of the

low-density-lipoprotein receptor (LDL-R) family act as receptors for the minor group. The

binding site of ICAM-1 on the major group HRV, such as HRV16, is located in the canyon (*6*)

(*7*). This is the same area where poliovirus receptor binds (Fig. 6.1) (*8*). Receptor binds into the

canyon, which destabilizes the virus and initiates the uncoating process. The binding site of

very-low-density-lipoprotein receptor (VLDL-R) on the minor-group HRV, such as HRV2, is on

the mesa (Fig. 6.1) (*9*), not in the canyon like that of major-group HRVs. Receptors bind outside

the canyon and do not cause viral instability and the uncoating process of HRV2 is triggered at

the plasma membrane by acidification (*10*). The use of antibodies could show whether the N-

terminus of VP1 is externalized at the same site when the virus receptor binds to a same or

different position on the virus capsid. In other words, we should learn whether the

externalization of VP1 occurs similarly among viruses that have the same or different types of

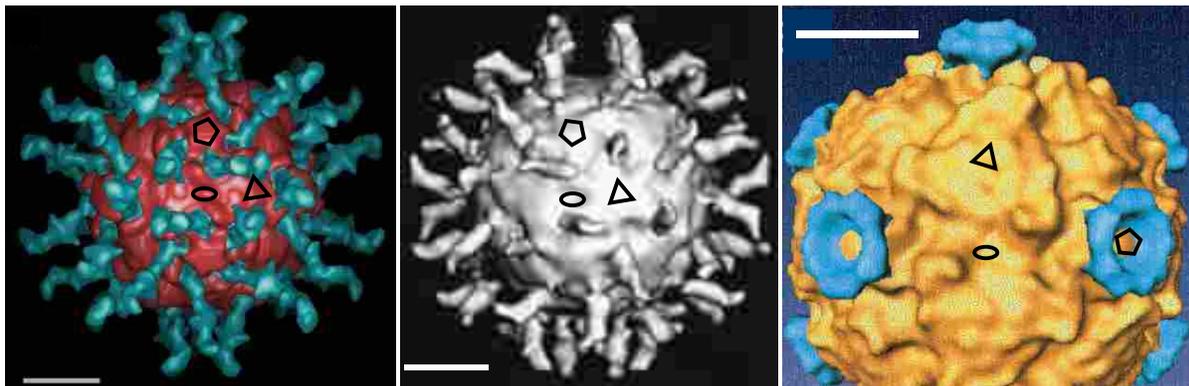receptors (i.e. same or different receptor-binding sites).

Figure 6.1. Cryo-EM image reconstructions of three complexes between picornaviruses and soluble fragments of

their receptors adapted from (*6, 8, 9*). Left panel: reconstruction of poliovirus (red) complexed with CD155 (blue).

Middle panel: reconstruction of the complex between HRV16 and ICAM-1. Right panel: reconstruction of the

complex between HRV2 with VLDL-R. Fivefold (pentagon), threefold (triangle) and twofold symmetry axes are

labeled. Bar =100 Å.

FHV is one of the notable members of the nodaviruses family. Nodaviruses comprise a family of small, icosahedral, non-enveloped, RNA viruses that naturally infect insects and fish (*11*). Similar to picornaviruses, nodaviruses enter cells via receptor-binding-induced endocytosis; the next step is virus uncoating by passing RNA across the endosomal membrane (*12*). Even though FHV belongs to the nodavirus family instead of the picornavirus family, its structural properties, such as the icosahedral, non-enveloped capsid, ssRNA genome, and the externalization of the internal peptides, is similar to poliovirus (*3*). The study of the externalization of internal peptides will show us if the poliovirus cell-entry model (e.g. the exposure of membrane-binding polypeptides) is suitable for other virus families. If so, this may suggest a general mechanism for non-enveloped virus cell-entry. It may also have applicability in other similar interactions of protein and membrane (non-viral interactions).

References

1. Bubeck, D., Filman, D. J., Cheng, N., Steven, A. C., Hogle, J. M., and Belnap, D. M. (2005) The structure of the poliovirus 135S cell entry intermediate at 10-Angstrom resolution reveals the location of an externalized polypeptide that binds to membranes, *J. Virol. 79*, 7745-7755.

2. Dove, A. W., and Racaniello, V. R. (2000) An antiviral compound that blocks structural transitions of poliovirus prevents receptor binding at low temperatures, *J Virol 74*, 3929-3931.

3. Bothner, B., Dong, X. F., Bibbs, L., Johnson, J. E., and Siuzdak, G. (1998) Evidence of viral capsid dynamics using limited proteolysis and mass spectrometry, *J Biol Chem 273*, 673-676.

4. Hewat, E. A., Neumann, E., and Blaas, D. (2002) The concerted conformational changes during human rhinovirus 2 uncoating, *Mol Cell 10*, 317-326.

5. Katpally, U., Fu, T. M., Freed, D. C., Casimiro, D. R., and Smith, T. J. (2009) Antibodies to the buried N terminus of rhinovirus VP4 exhibit cross-serotypic neutralization, *J Virol 83*, 7040-7048.

6. Kolatkar, P. R., Bella, J., Olson, N. H., Bator, C. M., Baker, T. S., and Rossmann, M. G. (1999) Structural studies of two rhinovirus serotypes complexed with fragments of their cellular receptor, *EMBO J 18*, 6249-6259.

7. Olson, N. H., Kolatkar, P. R., Oliveira, M. A., Cheng, R. H., Greve, J. M., McClelland, A., Baker, T. S., and Rossmann, M. G. (1993) Structure of a human rhinovirus complexed with its receptor molecule, *Proc Natl Acad Sci U S A 90*, 507-511.

8. Belnap, D. M., McDermott, B. M., Jr., Filman, D. J., Cheng, N., Trus, B. L., Zuccola, H. J., Racaniello, V. R., Hogle, J. M., and Steven, A. C. (2000) Three-dimensional structure of poliovirus receptor bound to poliovirus, *Proc. Natl. Acad. Sci. USA 97*, 73-78.

9. Neumann, E., Moser, R., Snyers, L., Blaas, D., and Hewat, E. A. (2003) A cellular receptor of human rhinovirus type 2, the very-low-density lipoprotein receptor, binds to two neighboring proteins of the viral capsid, *J Virol 77*, 8504-8511.

10. Brabec, M., Baravalle, G., Blaas, D., and Fuchs, R. (2003) Conformational changes, plasma membrane penetration, and infection by human rhinovirus type 2: role of receptors and low pH, *J Virol 77*, 5370-5377.

11. Schneemann, A., Reddy, V., and Johnson, J. E. (1998) The structure and function of nodavirus particles: a paradigm for understanding chemical biology, *Adv Virus Res 50*, 381-446.

12. Bong, D. T., Steinem, C., Janshoff, A., Johnson, J. E., and Reza Ghadiri, M. (1999) A highly membrane-active peptide in Flock House virus: implications for the mechanism of nodavirus infection, *Chem Biol 6*, 473-481.